



HAL
open science

Flagella-like beating of actin bundles driven by self-organized myosin waves

Marie Pochitaloff, Martin Miranda, Mathieu Richard, Atitheb Chaiyasitdhi, Yasuharu Takagi, Wenxiang Cao, Enrique de la Cruz, James Sellers, J.-F. Joanny, Frank Jülicher, et al.

► **To cite this version:**

Marie Pochitaloff, Martin Miranda, Mathieu Richard, Atitheb Chaiyasitdhi, Yasuharu Takagi, et al.. Flagella-like beating of actin bundles driven by self-organized myosin waves. *Nature Physics*, 2022, 18 (10), pp.1240. 10.1038/s41567-022-01688-8. hal-03748988

HAL Id: hal-03748988

<https://hal.science/hal-03748988v1>

Submitted on 10 Aug 2022

HAL is a multi-disciplinary open access archive for the deposit and dissemination of scientific research documents, whether they are published or not. The documents may come from teaching and research institutions in France or abroad, or from public or private research centers.

L'archive ouverte pluridisciplinaire **HAL**, est destinée au dépôt et à la diffusion de documents scientifiques de niveau recherche, publiés ou non, émanant des établissements d'enseignement et de recherche français ou étrangers, des laboratoires publics ou privés.

1 **Flagella-like beating of actin bundles driven by self-**
2 **organized myosin waves.**

3 Marie Pochitaloff^{1,†}, Martin Miranda², Mathieu Richard¹, Atitheb Chaiyasitdhi¹, Yasuharu
4 Takagi³, Wenxiang Cao⁴, Enrique M. De La Cruz⁴, James R. Sellers³, Jean-François Joanny^{1,5},
5 Frank Jülicher^{2,6}, Laurent Blanchoin^{7,8}, Pascal Martin^{1*}

6
7 ¹*Laboratoire Physico-Chimie Curie, Institut Curie, Université PSL, Sorbonne Université,*
8 *CNRS UMR168, F-75248 Paris, France.*

9 ²*Max Planck Institute for the Physics of Complex Systems, 01187 Dresden, Germany.*

10 ³*Laboratory of Molecular Physiology, National Heart, Lung and Blood Institute, NIH,*
11 *Bethesda, MD 20892, USA*

12 ⁴*Department of Molecular Biophysics and Biochemistry, Yale University, New Haven, CT*
13 *06520-8114, USA*

14 ⁵*Collège de France, 11 place Marcelin Berthelot 75231 Paris Cedex 05, France*

15 ⁶*Cluster of Excellence Physics of Life, Technische Universität Dresden, 01062 Dresden,*
16 *Germany*

17 ⁷*CytomorphoLab, Biosciences and Biotechnology Institute of Grenoble, Laboratoire de*
18 *Physiologie Cellulaire & Végétale, Université Grenoble-Alpes/CEA/CNRS/INRA, 38054*
19 *Grenoble, France*

20 ⁸*CytomorphoLab, Hôpital Saint Louis, Institut Universitaire d'Hématologie, UMRS1160,*
21 *INSERM/AP-HP/Université Paris Diderot, 75010 Paris, France*

22 [†]*Present address: Department of Mechanical Engineering, UC Santa Barbara, 93106-5070*
23 *Santa Barbara, USA.*

24 **To whom correspondence should be addressed: Email: pascal.martin@curie.fr*

25

26 **ABSTRACT:** Wave-like beating of eukaryotic cilia and flagella—threadlike protrusions
27 found in many cells and microorganisms—is a classic example of spontaneous mechanical
28 oscillations in biology. This type of self-organized active matter raises the question of the
29 coordination mechanism between molecular motor activity and cytoskeletal filament bending.
30 Here we show that in the presence of myosin motors, polymerizing actin filaments self-
31 assemble into polar bundles which exhibit wave-like beating. Importantly, filament beating is
32 associated with myosin density waves initiated at twice the frequency of the actin bending
33 waves. A theoretical description based on curvature control of motor binding to the filaments
34 and of motor activity explains our observations in a regime of high internal friction. Overall,
35 our results indicate that the binding of myosin to actin depends on the actin-bundle shape,
36 providing a feedback mechanism between myosin activity and filament deformations for the
37 self-organization of large motor-filament assemblies.

38

39 **Introduction**

40 Biological systems can self-organize at large scales by orchestrating the local activity of many
41 small constituents that each consume energy from the environment. The regular beating patterns
42 exhibited by cilia and flagella provide a prototypical example of such self-organization. Using
43 an in-vitro biomimetic approach, we study here minimal requirements for the emergence of
44 spontaneous beating of polar bundles of bio-filaments driven by molecular motors.

45 Cilia and flagella of eukaryotes ranging from single cells to complex organisms share a
46 complex common structure—the axoneme. The axoneme comprises a cylindrical arrangement
47 of parallel filaments called microtubules, about 10,000 dynein motors uniformly distributed
48 along the microtubules^{1,2}, as well as hundreds of other proteins³. Importantly, the flagellar
49 beat—a regular oscillatory pattern of propagating bending waves—requires coordination of the
50 motors both in time and along the length of the axoneme^{2,4,5}. The dynamics of flagellar beating
51 is a classical problem of theoretical biophysics. Many models have been developed to describe
52 the feedback mechanisms specifying how the activity of the molecular motors depends on the
53 filament-bundle shape⁴⁻¹³. However, the coupling between motor activity and flagellar beating
54 is still a matter of debate². In addition, although dissipation from external hydrodynamic drag
55 on the flagellar outer surface is usually thought to balance power input from the motors, the
56 contribution of internal sources of friction has recently been discussed¹⁴⁻¹⁶.

57 Biomimetic in-vitro experiments with purified proteins¹⁷⁻¹⁹ have demonstrated that
58 spontaneous oscillations can emerge in motor ensembles under elastic loading, without the
59 intervention of regulatory proteins or the external drive of an oscillatory biochemical signal.
60 These experiments confirmed the predicted existence of generic oscillatory instabilities in
61 motor systems^{11,20,21}. In contrast to top-down approaches on functional cilia or flagella, in-vitro
62 experiments afford an attractive means to control physical parameters such as the size of the
63 system, geometrical constraints, or the properties of the motors at work, and thus to probe the
64 physical underpinning of motor coordination in oscillatory systems.

65 In this work, we present a bottom-up approach based on a minimal active molecular system.
66 We show that, in the presence of myosin motors, polymerizing actin filaments can self-
67 assemble in vitro into polar bundles of filaments that spontaneously exhibit wave-like beating.
68 The beating properties in this artificial system resemble those of eukaryotic flagella, despite the
69 different molecular identity of the filaments and motors at work and despite the lack of
70 regulatory proteins. We used surface micro-patterns of actin nucleators to control the geometry
71 of actin-bundle formation in the presence of myosin motors. We analysed the properties of the
72 emerging actin-bending waves as a function of the size of the actin bundle and of the identity

73 of the myosin motors that drive the oscillations. Importantly, we demonstrate that actin-bending
74 waves are associated with myosin-density waves: myosin recruitment and localization on the
75 actin bundle are dynamically coupled to the actin-bundle shape. A theoretical description based
76 on curvature control of motor binding to the filaments and of motor activity explains our
77 observations in a regime of high internal friction.

78 **Results**

79 We used surface micro-patterns—disks—of a nucleation-promoting factor to control the
80 geometry and collective organization of actin polymerization^{22–24}. Because of steric
81 interactions, actin filaments grow perpendicular to the circular borders of the actin-nucleation
82 zone by monomer addition to their barbed ends, resulting in radial polar networks of filaments
83 (Supplementary Fig. 1). Previous work has demonstrated that the length of the actin filaments
84 is exponentially distributed, with a mean length of about 8 μm ²⁴. Inclusion of a depleting agent
85 ensured that most of the filaments grew parallel to the substrate and that the network remained
86 within a few hundred nanometers of the passivated glass surface²⁵; the depleting agent also
87 facilitated bundle formation²⁶. We performed the in-vitro polymerization assay in the presence
88 of either heavy meromyosin II, which is a soluble two-headed fragment of skeletal muscle
89 myosin II—hereafter called myosin II for simplicity, or of a two-headed fragment of myosin
90 Va fused to the green-fluorescent protein—hereafter called myosin V. We found that growing
91 actin filaments in the presence of myosin motors self-organized into bundles with a diameter
92 that decreased from their proximal to their distal ends (Extended Data Fig. 1). Remarkably, the
93 actin-filament bundles displayed periodic bending waves traveling from the base towards the
94 tip of the bundle (Extended Data Fig. 1; Supplementary Videos 1-3). In the following, the index
95 'II' and 'V' refer to data obtained with myosin-II and myosin-V motors, respectively. Unless
96 otherwise indicated, we provide averages and standard deviations (SD) of beating-bundle
97 properties over ensembles of n bundles.

98 **Actin-bending waves driven by myosin II.** We analysed the beating properties of
99 fluorescently-labelled actin bundles after 23 ± 8 min (mean \pm SD; $n = 59$) of polymerization.
100 At this time, the bundles had grown to a length $L_{II} = 15.9 \pm 6.1$ μm ($n = 59$). Automatic
101 tracking of the center line of an actin-filament bundle (Fig. 1a; Supplementary Video 4)
102 revealed beating patterns with a heart-shaped envelope in which the bundle's tip follows a
103 characteristic 8-figure (Fig. 1b). These patterns resemble those reported for flagella of the bull
104 sperm^{27,28} but with slower beating kinetics. At any given arc length s , the angle $\psi(t, s)$ between
105 the tangent to bundle's center line and the vertical axis (axis Y in Fig. 1c) displayed sinusoidal

106 oscillations as a function of time t (Fig. 1c-d) with a period $T_{II} = 15 \pm 9$ s ($n = 59$). The
107 oscillation amplitude ψ_0 increased linearly from the base of the bundle to typically two-thirds
108 of the total length at a rate $\psi'_0 = 12.5 \pm 3.4$ deg/ μm ($n = 59$), before saturating (Fig. 1d) and
109 reaching a maximum value $\psi_{MAX} = 127 \pm 11$ deg ($n = 46$). Saturation was observed only
110 when the bundle was long enough, typically $L_{II} > 11$ μm (Extended Data Fig. 2). The phase
111 $\phi(s)$ of the tangent-angle oscillation decreased from the base ($s = 0$) to the tip ($s = L$) of the
112 bundle, with a nearly linear relationship of slope ϕ' over most of the bundle's length (Fig. 1e).
113 As a result, the wavelength $\lambda_{II} = -2\pi/\phi' = 17.1 \pm 5.8$ μm ($n = 59$) and the velocity $v_{II} =$
114 $\lambda_{II}/T_{II} = 1.4 \pm 0.8$ $\mu\text{m/s}$ ($n = 59$) of the corresponding traveling wave were nearly uniform
115 along the bundle. A color plot of $\psi(t, s)$ recapitulates these observations; propagation of actin-
116 bending waves at uniform velocities is visualized by linear iso-color lines (Fig. 1f). Wave
117 propagation at uniform velocities is remarkable considering that the actin bundles are about one
118 micrometer thick near their base, where they comprise hundreds of filaments, and get
119 progressively thinner towards their tip, where they end with a single or only a few filaments.
120 As discussed in Supplementary Information, bending-wave propagation at uniform velocity
121 despite the structural heterogeneity of the filament bundle is most easily explained if an internal
122 source of friction dominates external viscous drag on the bundle. Uniform wave velocities are
123 also often observed in eukaryotic flagellar systems (e.g. ⁵), but these flagella are based on a
124 homogeneous axonemal structure comprising nine doublets of microtubules along most of the
125 flagellar length.

126 The actin-filament bundles generally remained in focus within the observation plane of the
127 spinning-disk microscope, indicating that the beating motion was almost planar. However,
128 weak blinking of the actin-fluorescence intensity at a given arc length betrayed a small out-of-
129 plane component to the beat that could result in oscillations of the projected bundle length
130 (Extended Data Fig. 3, Supplementary Video 5). We analysed here the shape of the beat pattern
131 within the plane of the beat.

132 **Actin-bending waves driven by myosin V.** To evaluate the generality of self-organized
133 beating in polar bundles of actin filaments driven by myosin motors, we also performed
134 experiments with myosin-V motors. Myosin II and myosin V are both double-headed molecular
135 motors with movements directed toward the barbed ends of the actin filaments, thus away from
136 the nucleation disks of actin polymerization. However, their biophysical properties and in-vivo
137 functions differ strongly ²⁹: myosin II is a non-processive motor that normally works in large

138 groups to mediate muscle contraction, whereas myosin V is a processive motor that usually
139 operates at the level of a single dimer or of a few dimers.

140 Despite these differences, we found that polar actin networks could also self-assemble into
141 wave-like beating bundles under the action of myosin V (Fig. 2; Supplementary Videos 2 and
142 3). The heart-shaped beating patterns and 8-figures with myosin V were similar to those
143 obtained with myosin II. Over an ensemble of $n = 29$ beating bundles of length
144 $L_V = 18.3 \pm 5.4 \mu\text{m}$, actin-bending waves of wavelength $\lambda_V = 15.9 \pm 3.5 \mu\text{m}$ travelled at
145 nearly uniform velocities from bundle's base toward its tip, while the magnitude ψ_0 of tangent-
146 angle oscillations grew along the length of the bundle at a rate $\psi'_0 = 18.9 \pm 3.6 \text{ deg}/\mu\text{m}$ before
147 reaching a maximum $\psi_{MAX} = 133 \pm 11 \text{ deg}$. There is no statistical difference between the
148 mean values of the bundle length and wavelength for myosin-II and myosin-V motors but the
149 amplitude of tangent-angle oscillation increased more steeply with the arc length and the
150 maximal tangent angle was slightly larger for myosin V (Table 1). The most striking difference
151 between the two motor types was in the kinetics of the beating movements. Myosin V is known
152 to be a slower motor than myosin II³⁰. Accordingly, tangent-angle oscillations and the
153 propagation of actin-bending waves were about 4-fold slower with myosin V (Fig. 2d; Table 1),
154 corresponding to a period $T_V = 54 \pm 27 \text{ s}$ ($n=29$) and a travelling-wave velocity $v_V = 0.37 \pm$
155 $0.15 \mu\text{m/s}$ ($n = 29$).

156 **Effects of bundle length on beating properties.** We observed self-organized beating for
157 actin-filament bundles with a length L that ranged between $6 \mu\text{m}$ and $40 \mu\text{m}$. Over this range,
158 the wavelength λ of the bending waves displayed a positive correlation with the bundle length
159 (Fig. 3a), both with myosin II (Pearson test: $r = 0.72$; p-value: $1.7 \cdot 10^{-10}$) and with myosin V
160 (Pearson test: $r = 0.36$; p-value: $1.1 \cdot 10^{-3}$). Longer bundles showed longer wavelengths and the
161 wavelength was on average nearly equal to the bundle length (Table 1). In ensemble averages,
162 the oscillation period of the tangent angle displayed a weak positive correlation with the bundle
163 length with myosin V (Pearson's test: $r = 0.36$; p-value = 0.05) but no significant correlation
164 with myosin II (Pearson's test: $r = 0.2$; p-value = 0.13). However, because the beating actin
165 bundles elongate at a velocity of $0.8 \pm 0.5 \mu\text{m}/\text{min}$ ($n = 14$) as polymerization proceeds, our in-
166 vitro assay provides an attractive means to probe, in a single experiment, how the beating
167 properties change with the bundle length while all other parameters remained fixed (Fig. 3b and
168 c; Supplementary Video 6). With myosin II, beating was fast enough that the actin bundle length
169 remained nearly constant over a few tens of oscillation cycles (Fig. 3b). In this case, we
170 observed that the period of tangent-angle oscillation increased with the bundle's length at a

171 mean rate of 0.9 ± 0.7 s/ μm ($n = 5$). In agreement with the observed increase of the wavelength
172 with the bundle length (Fig. 3a), the travelling velocity of the actin-bending waves stayed nearly
173 the same over the range of bundle length that we could explore (insert in Fig. 3c).

174 **Interplay between actin-bending and myosin-density waves.** Because myosin V was
175 fused to the green-fluorescent protein (GFP), we could visualize the motors during wave-like
176 beating of actin bundles (Supplementary Videos 7-9). In contrast to the monotonically
177 decreasing and stationary actin-density profiles (Extended Data Fig. 4a), the myosin-density
178 profiles exhibited a peak that appeared abruptly near the bundle's base and then travelled toward
179 the bundle's tip, corresponding to a myosin-density wave (Fig. 4a). Thus, although they were
180 added in bulk at a homogeneous concentration, the motors did not decorate the actin bundle
181 according to the local actin density but were instead enriched within an apical region of the
182 bundle. The myosin-fluorescence signal was elongated, conformed to the local shape of the
183 bundle, and thus followed the bundle movement (Extended Data Fig. 5a). The myosin-density
184 peak remained within a restricted region of the observation plane near the center of the 8-figure
185 drawn by the bundle's tip (Extended Data Fig. 5b). As a result, when the beating bundle grew
186 in length, the myosin-density peak moved together with the 8-figure (Supplementary Video 9;
187 Extended Data Fig. 5c-d). Interestingly, plotting the ratio of myosin- and actin-density profiles
188 revealed an increase of the motor density per actin filament during wave propagation (Extended
189 Data Fig. 4b). The arc length at which the myosin density was maximal (Fig. 4d-e) displayed a
190 sawtooth-shaped oscillation as a function of time. These observations suggest that myosin
191 motors were periodically recruited in a proximal region of the filament bundle and released at
192 the bundle's tip.

193 To describe how the myosin-density waves were coupled to the underlying actin-bending
194 waves, we compared the myosin-density profiles (Fig. 4a and d) to the bundle-curvature
195 profiles (Fig. 4b and c; Supplementary Video 10). By repeating these measurements over an
196 ensemble of beating bundles, we observed that the myosin waves were produced at precisely
197 twice the frequency of actin-bending waves, corresponding to periods of 20.7 ± 6.0 s and
198 41.1 ± 12.4 s ($n = 10$), respectively. The velocity $v_V^{myo} = 0.7 \pm 0.2$ $\mu\text{m/s}$ ($n = 17$) of the
199 myosin waves was 1.4 to 3 times the velocity reported for myosin-V transport in in-vitro gliding
200 or bead assays³¹⁻³³ but comparable to that of in-vitro processive movements of single myosin-
201 V molecules on actin filaments³⁴ and to transport velocities measured inside cells³⁵. The
202 myosin-density peak may travel towards the bundle's tip because the attached motors move
203 processively along the actin filaments, or because motors continuously bind to the front and
204 unbind from the rear of a travelling motor collection, or both. Because myosin recruitment did

205 not happen at the very base of the actin bundle but at a more apical position, the velocity of the
206 myosin waves was on average only 1.7-fold larger than the velocity $v_V^{act} = 0.42 \pm 0.15 \mu\text{m/s}$
207 ($n = 17$) of the corresponding actin bending waves.

208 Superimposing the myosin-density profiles (Fig. 4a) and the actin curvature profiles
209 (Fig. 4b) provides the envelopes of the two interrelated waves. The amplitude of the actin-
210 bundle curvature wave increased smoothly as the wave travelled from the bundle's base towards
211 its tip before saturating. In contrast, the corresponding myosin density increased abruptly at a
212 position $s^* = 6.9 \pm 1.8 \mu\text{m}$ where the actin curvature reached a threshold value $C^* = 0.65 \pm$
213 $0.09 \mu\text{m}^{-1}$, as measured over an ensemble of $n = 14$ beating bundles. This observation
214 suggests that myosin recruitment from the bulk to the actin-filament bundle depends on the
215 magnitude of the bundle's local curvature. At the time of recruitment, the myosin peak was
216 localized near a position of maximal absolute curvature in the actin bundle (Fig. 4e, Extended
217 Data Fig. 4; Supplementary Videos 7 and 10). At later times, while the waves continued
218 traveling towards the bundle's tip, both the actin curvature and the myosin density remained at
219 saturated values (Fig. 4a and b). However, because myosin waves travelled faster than actin-
220 curvature waves, the myosin peak did not colocalize with the position of maximal absolute actin
221 curvature but was positioned farther toward the bundle's tip (Fig. 4c-e, Extended Data Fig. 6).
222 We note that the ratio of the standard deviation to the mean for the threshold curvature C^* was
223 small, only 14%. Over the same ensemble of beating bundles, the bundle width $W^* = 0.66 \pm$
224 $0.09 \mu\text{m}$ ($n = 14$) at the position s^* of myosin recruitment also showed small variations,
225 indicating that the beating bundles were similar in our experiments.

226 Thus, visualization of the motors revealed a nonlinear self-organization process. Bending
227 waves of the actin-filament bundles are associated with myosin-density waves generated at
228 twice the frequency of bending oscillations. In the following, we present a theory showing how
229 wave-like beating of an active filament bundle may emerge from a dynamic interplay between
230 bending of the bundle and curvature-dependent motor binding to the filaments.

231 **Physical description of self-organized beating.** To account for our experimental
232 observations, we built a coarse-grained theory of an active filament bundle that generates wave-
233 like beating through a dynamic instability (Supplementary Information). The theory keeps track
234 of a minimal set of mesoscopic variables as a function of time t and the arc length s : the angle
235 $\psi(t, s)$ between the tangent to the center line of the bundle and the vertical axis, which describes
236 the shape of the bundle, the total lineic density $\rho(t, s)$ of bound motors, and the algebraic lineic
237 density $\rho_a(t, s)$ of active motor crosslinks that generate internal torques within the bundle. The

238 dynamic equations for these variables are obtained from symmetry arguments and conservation
239 laws.

240 The active torques that drive beating are generated by motors that form transient crosslinks
241 between filaments. A motor-mediated crosslink between a filament pair can produce a
242 clockwise or an anticlockwise torque, depending on whether the motor advances on one or the
243 other filament of the pair. We denote by $\rho_+(t, s)$ and $\rho_-(t, s)$ the corresponding lineic densities
244 of active crosslinks in a cross-section of the filament bundle and we define the algebraic lineic
245 density $\rho_a(t, s) = (\rho_+ - \rho_-)/N(s)$ of active crosslinks per filament. The bundle is a
246 heterogeneous structure comprising aligned polar filaments of different lengths. The number
247 $N(s)$ of filaments in a cross-section decreases exponentially with the arc length s . The net active
248 torque at arc length s is given by $N(s)A_0\rho_a(t, s)$, where A_0 is the magnitude of the torque
249 produced by an active crosslink. Here we propose that the active torque per filament and per
250 unit length increases at a rate A_0k_aC proportional to bundle curvature $C = \partial_s\psi$ and relaxes at
251 a rate k_d . A linear relation is expected if the radius of curvature of the bundle is larger than the
252 diameter of the bundle's cross-section. The parameter k_a characterizes the curvature
253 dependence of the active torque. This coupling generates a positive feedback between torque
254 and curvature. Because of the delay due to binding and unbinding kinetics of active crosslinks,
255 the active filament bundle can undergo an oscillatory instability—a Hopf bifurcation—beyond
256 a critical value Ω_c of the control parameter $\Omega = A_0 k_a/k_d$, resulting in the emergence of wave-
257 like beating.

258 Beating of the filament bundle is associated with a density wave of bound motors $\rho(t, s)$,
259 with abrupt motor recruitment beyond a threshold value of bundle curvature $C = C^*$. Because
260 recruitment happens near the base of the filament bundle and is followed by propagation of a
261 motor-density peak of constant amplitude, we propose that $C^* = C_0/N(s)$ is inversely related
262 to the local number of filaments: the larger the local number of filaments, the easier it is to
263 recruit motors upon bundle bending at this position. The mechanosensitivity of motor binding
264 is thus a cooperative behavior of the filament bundle. Finally, we consider the simple limit in
265 which dissipation is dominated by internal shear friction, with a friction coefficient per filament
266 ξ_0 , and that viscous drag by the surrounding fluid only provides a small contribution (see
267 Section 6 in the Supplementary Information). This limit is valid for sufficiently short bundles.
268 In this regime of high internal friction, the dynamic equation for $\psi(t, s)$ depends only weakly
269 on the number of filaments in the bundle.

270 At the Hopf bifurcation ($\Omega = \Omega_c$), wave-like beating emerges at a frequency $\omega_c \simeq$
271 $k_d \sqrt{\frac{2\pi^2}{L^2} \frac{\kappa_0}{\xi_0 k_d} + 1}$, in which L is the bundle length and κ_0 the bending rigidity per filament. For
272 parameter values listed in Supplementary Tables S1 and S2, our numerical solutions show
273 bending waves travelling from the base to the tip of the bundle at a nearly uniform velocity over
274 most of the bundle's length and beating patterns with characteristic 8-figures (Fig. 5a-d).
275 Curvature waves (Fig. 5e) are associated with motor-density waves (Fig. 5f; Supplementary
276 Video 11). The motors bind to the filaments near the base of the bundle at twice the frequency
277 of the bending oscillations. Motor binding corresponds to the sudden appearance of a localized
278 motor-density peak $\rho(t, s)$ where and when the bundle reaches a threshold curvature (Fig. 5g).
279 The motor-density wave then travels with a nearly constant magnitude towards the bundle's tip,
280 with a velocity larger than that of the curvature wave (Fig. 5h). As in experiments, the myosin-
281 density peak remained within a restricted region of the XY plane, near the center of the 8-figure
282 in the beat pattern (Extended Data Figs. 5b and 7).

283 Overall, a simple model based on nonlinear curvature control of motor binding, on curvature
284 control of active-torque generation, and on high internal shear friction captures the key features
285 of the complex interplay between actin bending waves and myosin-density waves observed in
286 experiments.

287

288 **Discussion**

289 Using a bottom-up approach based on a minimal active molecular system, we have
290 demonstrated here that wave-like beating emerges robustly in polar bundles of actin filaments
291 and myosin motors. In the presence of myosin-motor dimers added in bulk, growing actin
292 filaments self-organize into beating bundles. Beating takes the form of bending waves with
293 shapes resembling those observed in eukaryotic cilia and flagella, as well as in reconstituted
294 kinesin-microtubule systems¹⁹, despite the different families of filaments and motors at work.
295 Thus, our finding provides further evidence that the emergence of wave-like oscillations is a
296 generic feature of motor-filament systems, irrespective of the molecular details, providing
297 experimental support for general theories of this form of active matter^{11,21}.

298 Our assay is based on protein micropatterning, which allows to control the self-assembly of
299 actin-filament bundles and their spatial organization. In addition, visualization of the motors
300 while the actin bundle is beating revealed that actin-bending waves are associated with myosin-
301 density waves: the motor density increased abruptly beyond a threshold value of the bundle
302 curvature before travelling towards the tip of the actin bundle (Fig. 4). These observations
303 suggest that the filament-bundle shape regulates myosin *attachment* to actin, which could
304 provide a feedback mechanism between motor activity and filament bending^{8,9}. This
305 mechanism contrasts with shape-dependent *detachment* as the basis of a dynamic instability
306 that can give rise to spontaneous oscillations^{5,36,37}, although the two mechanisms are not
307 mutually exclusive.

308 How could the motors' affinity for the filaments depend on the filament-bundle shape? There
309 is a growing bulk of evidence showing that actin filaments are endowed with conformational
310 plasticity³⁸⁻⁴⁰ and that protein binding can stabilize a specific conformational state of actin as
311 shown for myosin-V⁴¹, in direct relevance to our work, as well as for other proteins^{42,43}. Strong
312 binding of myosin II has also been shown to reduce the helical angle of F-actin, elongating the
313 filament⁴⁴. Actin filaments therefore can act as mechanosensors because an applied force that
314 alters their conformation should also affect their affinity for actin-binding proteins^{40,45-48}.
315 Myosin motor molecules are actin-binding proteins that can actively exert a physical stress on
316 the filaments by converting energy from a biochemical fuel (here ATP) into mechanical work.
317 Tension of only a few piconewtons—a magnitude comparable to that exerted by a single myosin
318 motor³⁰—appears to be strong enough to distort the actin-filament structure⁴⁹. Thus, the actin
319 filament does not operate simply as a passive cable to which proteins can bind but can provide
320 feedback on protein binding and activity.

321 We have shown on general theoretical grounds that a positive feedback between curvature
322 and active torque generation by the motors is sufficient for the emergence of self-organized
323 bending waves in a polar-filament bundle (Fig. 5; Supplementary Information). This feedback
324 mechanism is the simplest allowed by symmetry to linear order. Introducing nonlinearities that
325 account for the observed curvature dependence of myosin binding, the theory reproduces
326 quantitatively the main features of the experimental curvature and motor-density waves (Figs. 4
327 and 5, Supplementary Videos 7, 8, and 11). Curvature control of motor activity had earlier been
328 proposed to mediate motor coordination in eukaryotic flagella ^{8,9}, in particular to account for
329 waveforms in isolated *Chlamydomonas* axonemes ^{12,16}. In our work, curvature control is
330 described as an emergent behavior at a coarse-grained level based on symmetry arguments. As
331 in studies of the flagellar beat that also invoke such feedback, we do not address here the
332 detailed molecular mechanism by which the motors sense curvature of the filament bundle. This
333 question remains a key open challenge in all these systems in view of the small estimated strains
334 resulting from curvature changes in the filaments ¹². In addition, we cannot preclude that
335 regulation of motor activity in our assay also involves other phenomena. In particular in the
336 case of eukaryotic flagella a regulation by shear forces resulting from the interfilament sliding
337 ^{4,5,11} or by transverse forces from variations of the interfilament lateral distance—a mechanism
338 known as ‘geometric clutch’ ² have been invoked. Such concepts could also be relevant to motor
339 regulation in the assay studied here. Finally, future experiments ought to characterize the nature
340 of individual motor motion within the myosin-density waves, test how curvature control of
341 myosin binding depends on the number of filaments in the bundle, and determine quantitatively
342 the relative importance of internal and external contributions to friction as a function of the
343 architecture of the bundle.

344 In conclusion, our in-vitro work with a minimal acto-myosin system shows that the
345 emergence of self-organized bending waves is a generic feature of motor-filament systems. We
346 shed light on the dynamic interplay between myosin binding, myosin activity and the filament-
347 bundle shape, opening an avenue for understanding the self-organization of this type of active
348 matter.

349

350 **Acknowledgements:**

351 We are indebted to M. Rief for providing the heavy meromyosin II molecules. We thank the
352 Cell and Tissue Imaging core facility (PICT-IBiSA) of the Institut Curie, a member of the
353 French National Research Infrastructure France-BioImaging (ANR10-INBS-04). We thank
354 John Manzi for protein purification and characterization, Fahima Di Federico for the genetic
355 construct of His-pWA-Streptavidin, Jean-Yves Tinevez, Antoine Allard, and Isabelle Bonnet
356 for help with Matlab programming, Hajer Ennomani and Christophe Guérin for help with actin
357 micropatterning, and Julie Plastino and Cécile Sykes for fruitful discussions. This work was
358 supported by the French National Agency for Research (ANR-12-BSV5 0014; awarded jointly
359 to P.M. and L.B.), by the Labex Cell(n)Scale ANR-11-LABX-0038 and aNR-10-IDEX-001-
360 02, by the United States National Institutes of Health Grant R35-GM135656 (awarded to E. M.
361 D. L. C.), and by the European Research Council (741773 (AAA); awarded to L.B.).

362 **Author Contributions Statement**

363 M.P. and M.M. contributed equally to the work. M.P., M.M., M.R., A.C., J.F.J., F.J, L.B. and
364 P.M. designed research, performed research, and analyzed data. Y.T., W.C., E.D.L.C, and J.S.
365 provided new reagents. M.P., M.M., J.F.J, F.J., L.B, and P.M. wrote the manuscript.

366 **Competing Interests Statement**

367 The authors declare no competing interests.

368

Parameter	Definition	Myosin II (n = 59)	Myosin V (n = 29)	Statistical t-test
L (μm)	Bundle length	15.9 ± 6.1	18.3 ± 5.4	n.s.
λ (μm)	Wavelength of bending waves	17.1 ± 5.8	15.9 ± 3.5	n.s.
λ/L	Wavelength-Length ratio	1.1 ± 0.3	0.9 ± 0.3	**
ψ'_0 (deg/ μm)	Growth rate of tangent-angle oscillation	12.5 ± 3.4	18.9 ± 3.6	****
ψ_{MAX} (deg)	Maximal tangent angle	127 ± 11	133 ± 11	*
T (s)	Tangent-angle period	15 ± 9	54 ± 27	****
v ($\mu\text{m/s}$)	Bending-wave velocity	1.4 ± 0.8	0.37 ± 0.15	****

369 **Table 1: Beating characteristics and statistical testing.** The numerical values are given as
370 mean \pm standard deviation over an ensemble of n bundles. With myosin II, only 46 of the 59
371 bundles were long enough ($L > 11 \mu\text{m}$) to show saturation of the tangent angle; the value of
372 ψ_{MAX} was thus determined with those ($n = 46$). To compare the mean values obtained with the
373 two motor types, we used two-tailed unpaired Student's t-tests with Welch's correction. Stars
374 correspond to p-values with * $p < 0.05$, ** $p < 0.01$, *** $p < 0.001$, and **** $p < 0.0001$, whereas
375 'n.s.' ($p > 0.05$) indicates non-significant differences.

376 **FIGURE LEGENDS**

377

378 **Fig. 1 | Beating of an actin-filament bundle with myosin II.** **a**, Snapshots of the actin-
379 filament bundle. Yellow box: The bundle (arrowhead) has grown to a length $L = 14.8 \mu\text{m}$ from
380 a micro-patterned, actin-nucleation disk. **b**, Beating pattern resulting from automatic tracking
381 of the bundle's center line; same bundle as in **a**. The insert defines the tangent angle ψ at any
382 point M of a bundle's center line; the arc length origin $s = 0$ is at the bundle's base (point O).
383 **c**, Tangent angle $\psi(t, s)$ as a function of time t at the arc lengths $s = 5 \mu\text{m}$ (purple) and $s =$
384 $10 \mu\text{m}$ (magenta); the corresponding power-spectral densities are shown on the right and their
385 peaks indicate an oscillation period $T = 11.2 \text{ s}$. **d**, Amplitude $\psi_0(s) =$
386 $\sqrt{2\langle(\psi(t, s) - \langle\psi(t, s)\rangle)^2\rangle}$ of the tangent-angle oscillation as a function of the arc length s .
387 The growth rate in the linear portion of the curve is $\psi'_0 = 16.2 \text{ deg}/\mu\text{m}$. **e**, Phase ϕ of the
388 Fourier amplitude at the beating frequency as a function of the arc length s . The slope to a linear
389 fit to the relationship $\phi(s)$ provides the wavevector $q = 0.30 \text{ rad}/\mu\text{m}$, corresponding to the
390 wavelength $\lambda = 20.9 \mu\text{m}$ and the propagation velocity $v = \lambda/T = 1.9 \mu\text{m/s}$ of actin-bending
391 waves. **f**, Color plot of the tangent angle $\psi(t, s)$ as a function of time t and arc length s .
392

393 **Fig. 2 | Beating of an actin-filament bundle with myosin V.** **a**, Beating pattern. **b**,
394 Tangent-angle profile $\psi(s)$, defined as in Fig. 1b, at various times over one period of
395 oscillation, with a 2-s time interval between successive profiles. **c**, Color plot of the tangent
396 angle $\psi(t, s)$ as a function of time t and arc length s . The period of tangent-angle oscillation is
397 here $T = 30.6s$ and the actin-filament bundle has an average visible length $L = 18 \mu\text{m}$. **d**, Box
398 plots (25th and 75th percentiles in cyan; median values in red; whiskers indicate maximal and
399 minimal values) and data points for the period T of tangent-angle oscillations (top) and the
400 velocity v of bending waves (bottom) driven by myosin II (black disks) and myosin V (white
401 disks).

402

403 **Fig. 3 | Beating properties as a function of actin-bundle length.** **a**, Wavelength λ of actin-
404 bending waves as a function of the actin-bundle length L for beating bundles driven by myosin
405 II (black disks) or by myosin V (white disks). The dashed line is of slope unity. **b**, Color plots
406 of the tangent angle ψ to an actin bundle's center line as a function of the arc length s and time.
407 The four successive recordings were obtained with the same actin bundle. Each recording
408 started at different times with respect to the initiation of actin polymerization, as indicated on
409 top of each panel. Actin beating was here driven by myosin II and displayed stationary
410 properties over the 1-min duration of each recording. **c**, Period T of tangent-angle oscillations
411 and velocity v of actin bending waves (insert) as a function of the actin-bundle length L . The
412 red line represents a linear fit of slope 0.33 ± 0.12 s/ μm (95%-confidence bounds) to the
413 relationship $T(L)$. Error bars for L and T are standard deviations over the duration of each
414 recording. Error bars for v are 95%-confidence bounds to linear fits of the relationship $\phi(s)$
415 between the phase of tangent-angle oscillations and the arc length. Same actin bundle as in **c**.
416

417 **Fig. 4 | Interplay between myosin-V-density and actin-curvature waves.** **a**, Myosin-
418 density profiles (arbitrary units) during one period of a myosin-density wave, here 15.3 s. The
419 order of the line colors, from dark blue to red, indicates time progression over one period of the
420 myosin density waves with a 2-s time interval. **b**, Actin-curvature profiles during one period
421 of bending oscillation, here 30.6 s. The actin-curvature profiles associated with the myosin-
422 density profiles shown in **a** are shown using the same line colors. The grey areas in **a** and **b**
423 were obtained by superimposing myosin-density and actin-curvature profiles, respectively, over
424 22 periods of bending oscillations, revealing the envelopes of the corresponding waves. **c**,
425 Kymograph of actin-curvature profiles (arbitrary units). **d**, Kymograph of myosin-density
426 profiles (arbitrary units). In **a-d**, there is a 2 s-interval between two successive profiles. **e**, Arc
427 length as a function of time for the points along the bundle's center line at which the actin
428 curvature is maximal (red disks), minimal (blue disks), and at which the myosin density peaks
429 (black dots and line). For this bundle, the arc length $s^* = 8.3 \pm 0.9 \mu m$ at which myosin density
430 increases abruptly, corresponding to myosin recruitment in the actin bundle at a threshold
431 curvature $C^* = 0.63 \pm 0.09 \mu m^{-1}$, is marked by dashed lines in **a**, **b**, and **e**. The slope of the
432 rising phase in saw-tooth oscillations of myosin density provided here a speed $v_V^{myo} = 0.7 \pm$
433 $0.2 \mu m/s$. The standard deviations from the mean were here calculated over 29 periods of
434 myosin density waves.

435

436 **Fig. 5 | Wave-like beating in a model of an active filament bundle.**

437 **a**, Wave-like beating pattern of the bundle's center line. **b**, Tangent angle $\psi(s, t)$ to the center
438 lines shown in **a** as a function of the arc length s at successive values of time t over one period
439 of bending oscillation. **c**, Curvature profiles $C(s, t) = \partial_s \psi$ resulting from the tangent-angle
440 profiles $\psi(s, t)$ shown in **b**. **d**, Color plot of the tangent angle $\psi(s, t)$, revealing bending waves
441 travelling from the base towards the tip of the bundle at a velocity of $0.56 \mu\text{m/s}$ and beating
442 with a period of 30.6 s . The corresponding curvature waves $C(s, t)$ are associated with motor-
443 density waves $\rho(s, t)$, both of which are shown as kymographs in **e** and **f**, respectively. **g**,
444 Profiles $\rho(s, t)$ of the total density of bound motors. **h**, Arc length as a function of time of the
445 points along the bundle's center line at which the bundle curvature is maximal (red line),
446 minimal (blue line), and at which the motor density peaks (black solid line). The motor-density
447 peak travels at a velocity of $1.1 \mu\text{m/s}$. There is a 2.2 s -interval between two successive profiles
448 in **a-c** and **e-g**. The arc length $s = 7.2 \mu\text{m}$ at which the motor density increases abruptly,
449 corresponding to motor recruited in the actin bundle, is marked by a dashed line in **b**, **c**, and **f**.
450 In **a-c** and **g**, the order of the line colors, from dark blue to red, indicates time progression over
451 one period of the motor-density waves with a 2.2-s time interval. These results are numerical
452 solutions of Equations S1-7 with parameter values listed in Table S2 (Supplementary
453 Information).

454

455 **References**

- 456 1. Nicastro, D. The Molecular architecture of axonemes revealed by cryoelectron tomography.
457 *Science* **313**, 944–948 (2006).
- 458 2. Lindemann, C. B. & Lesich, K. A. Flagellar and ciliary beating: the proven and the possible.
459 *J. Cell Sci.* **123**, 519–528 (2010).
- 460 3. Pazour, G. J., Agrin, N., Leszyk, J. & Witman, G. B. Proteomic analysis of a eukaryotic
461 cilium. *J. Cell Biol.* **170**, 103–113 (2005).
- 462 4. Brokaw, C. J. Molecular mechanism for oscillation in flagella and muscle. *Proc. Natl. Acad.*
463 *Sci. USA* **72**, 3102–3106 (1975).
- 464 5. Riedel-Kruse, I. H., Hilfinger, A., Howard, J. & Jülicher, F. How molecular motors shape
465 the flagellar beat. *HFSP J* **1**, 192–208 (2007).
- 466 6. Machin, K. E. Wave propagation along flagella. *J. Exp. Biol.* **35**, 796–806 (1958).
- 467 7. Brokaw, C. J. Computer simulation of flagellar movement VIII: Coordination of dynein by
468 local curvature control can generate helical bending waves. *Cell Motil. Cytoskeleton* **53**,
469 103–124 (2002).
- 470 8. Brokaw, C. & Rintala, D. Computer simulation of flagellar movement. III. Models
471 incorporating cross-bridge kinetics. *J. Mechanochem. Cell* **3**, 77–86 (1975).
- 472 9. Hines, M. & Blum, J. J. Bend propagation in flagella. I. Derivation of equations of motion
473 and their simulation. *Biophys. J.* **23**, 41–57 (1978).
- 474 10. Lindemann, C. B. A ‘Geometric Clutch’ Hypothesis to explain oscillations of the axoneme
475 of Cilia and Flagella. *J. Theor. Biol.* **168**, 175–189 (1994).
- 476 11. Camalet, S. & Jülicher, F. Generic aspects of axonemal beating. *New J. Phys.* **2**, 24–24
477 (2000).
- 478 12. Sartori, P., Geyer, V. F., Scholich, A., Jülicher, F. & Howard, J. Dynamic curvature
479 regulation accounts for the symmetric and asymmetric beats of *Chlamydomonas* flagella.
480 *Elife* **5**, e13258 (2016).

- 481 13. Oriola, D., Gadêlha, H. & Casademunt, J. Nonlinear amplitude dynamics in flagellar
482 beating. *R. Soc. Open Sci.* **4**, 160698 (2017).
- 483 14. Mondal, D., Adhikari, R. & Sharma, P. Internal friction controls active ciliary oscillations
484 near the instability threshold. *Sci. Adv.* **6**, eabb0503 (2020).
- 485 15. Nandagiri, A. *et al.* Flagellar energetics from high-resolution imaging of beating patterns
486 in tethered mouse sperm. *eLife* **10**, e62524 (2021).
- 487 16. Geyer, V. F., Howard, J. & Sartori, P. Ciliary beating patterns map onto a low-dimensional
488 behavioural space. *Nat. Phys.* **18**, 332–337 (2022).
- 489 17. Bourdieu, L. *et al.* Spiral defects in motility assays: A measure of motor protein force. *Phys.*
490 *Rev. Lett.* **75**, 176–179 (1995).
- 491 18. Placais, P. Y., Balland, M., Guerin, T., Joanny, J. F. & Martin, P. Spontaneous oscillations
492 of a minimal actomyosin system under elastic loading. *Phys. Rev. Lett.* **103**, 158102 (2009).
- 493 19. Sanchez, T., Welch, D., Nicastro, D. & Dogic, Z. Cilia-like beating of active microtubule
494 bundles. *Science* **333**, 456–9 (2011).
- 495 20. Jülicher, F. & Prost, J. Spontaneous Oscillations of Collective Molecular Motors. *Phys.*
496 *Rev. Lett.* **78**, 4510–4513 (1997).
- 497 21. Guerin, T., Prost, J., Martin, P. & Joanny, J. F. Coordination and collective properties of
498 molecular motors: theory. *Curr. Opin. Cell Biol.* **22**, 14–20 (2010).
- 499 22. Reymann, A. C. *et al.* Nucleation geometry governs ordered actin networks structures. *Nat*
500 *Mater* **9**, 827–32 (2010).
- 501 23. Reymann, A. C., Guerin, C., They, M., Blanchoin, L. & Boujemaa-Paterski, R.
502 Geometrical control of actin assembly and contractility. *Methods Cell Biol.* **120**, 19–38
503 (2014).
- 504 24. Richard, M. *et al.* Active cargo positioning in antiparallel transport networks. *Proc Natl*
505 *Acad Sci USA* **116**, 14835–14842 (2019).

- 506 25. Letort, G. *et al.* Geometrical and mechanical properties control actin filament organization.
507 *PLoS Comput. Biol.* **11**, e1004245 (2015).
- 508 26. Köhler, S., Lieleg, O. & Bausch, A. R. Rheological characterization of the bundling
509 transition in F-actin solutions induced by methylcellulose. *PLoS ONE* **3**, e2736 (2008).
- 510 27. Gray, J. The movement of the spermatozoa of the bull. *J. Exp. Biol.* **35**, 96–108 (1958).
- 511 28. Rikmenspoel, R. Movements and active moments of bull sperm flagella as a function of
512 temperature and viscosity. *J. Exp. Biol.* **108**, 205 (1984).
- 513 29. De La Cruz, E. M. & Ostap, E. M. Relating biochemistry and function in the myosin
514 superfamily. *Curr. Opin. Cell Biol.* **16**, 61–67 (2004).
- 515 30. Howard, J. *Mechanics of Motor Proteins and the Cytoskeleton*. (Sinauer Associates, 2001).
- 516 31. Mehta, A. D. *et al.* Myosin-V is a processive actin-based motor. *Nature* **400**, 590–593
517 (1999).
- 518 32. Rief, M. *et al.* Myosin-V stepping kinetics: A molecular model for processivity. *Proc. Natl.*
519 *Acad. Sci. USA* **97**, 9482–9486 (2000).
- 520 33. Clemen, A. E. *et al.* Force-dependent stepping kinetics of myosin-V. *Biophys. J.* **88**, 4402–
521 10 (2005).
- 522 34. Sakamoto, T. *et al.* Neck length and processivity of myosin V. *J. Biol. Chem.* **278**, 29201–
523 7 (2003).
- 524 35. Pierobon, P. *et al.* Velocity, processivity, and individual steps of single myosin V molecules
525 in live cells. *Biophys. J.* **96**, 4268–75 (2009).
- 526 36. Howard, J. Mechanical signaling in networks of motor and cytoskeletal proteins. *Annu.*
527 *Rev. Biophys.* **38**, 217–34 (2009).
- 528 37. Ma, R., Klindt, G. S., Riedel-Kruse, I. H., Jülicher, F. & Friedrich, B. M. Active phase and
529 amplitude fluctuations of flagellar beating. *Phys. Rev. Lett.* **113**, 048101 (2014).

- 530 38. Egelman, E. H., Francis, N. & DeRosier, D. J. F-actin is a helix with a random variable
531 twist. *Nature* **298**, 131–5 (1982).
- 532 39. Galkin, V. E., Orlova, A., Schroder, G. F. & Egelman, E. H. Structural polymorphism in F-
533 actin. *Nat. Struct. Mol. Biol.* **17**, 1318–23 (2010).
- 534 40. Galkin, V. E., Orlova, A. & Egelman, E. H. Actin filaments as tension sensors. *Curr. Biol.*
535 **22**, R96-101 (2012).
- 536 41. Kozuka, J., Yokota, H., Arai, Y., Ishii, Y. & Yanagida, T. Dynamic polymorphism of single
537 actin molecules in the actin filament. *Nat. Chem. Biol.* **2**, 83–6 (2006).
- 538 42. McGough, A., Pope, B., Chiu, W. & Weeds, A. Cofilin changes the twist of F-actin:
539 implications for actin filament dynamics and cellular function. *J. Cell. Biol.* **138**, 771–81
540 (1997).
- 541 43. Risca, V. I. *et al.* Actin filament curvature biases branching direction. *Proc. Natl. Acad. Sci*
542 *USA* **109**, 2913–8 (2012).
- 543 44. Tsaturyan, A. K. *et al.* Strong binding of myosin heads stretches and twists the actin helix.
544 *Biophys. J.* **88**, 1902–10 (2005).
- 545 45. Jegou, A. & Romet-Lemonne, G. The many implications of actin filament helicity. *Semin.*
546 *Cell Dev. Biol.* **102**, 65–72 (2020).
- 547 46. Mei, L. *et al.* Molecular mechanism for direct actin force-sensing by α -catenin. *eLife* **9**,
548 e62514 (2020).
- 549 47. Winkelman, J. D., Anderson, C. A., Suarez, C., Kovar, D. R. & Gardel, M. L. Evolutionarily
550 diverse LIM domain-containing proteins bind stressed actin filaments through a conserved
551 mechanism. *Proc. Natl. Acad. Sci. USA* 202004656 (2020).
- 552 48. Sun, X. *et al.* Mechanosensing through Direct Binding of Tensed F-Actin by LIM Domains.
553 *Dev. Cell* **55**, 468-482.e7 (2020).

554 49. Shimosawa, T. & Ishiwata, S. Mechanical distortion of single actin filaments induced by
555 external force: detection by fluorescence imaging. *Biophys. J.* **96**, 1036–44 (2009).
556

557 **Methods**

558 **Micropatterning of an actin nucleation-promoting factor.** The fusion protein His-pWA-
559 Streptavidin (also called S-pVCA) was produced and characterized following a published
560 protocol⁵⁰; the histidine tag (His) was used for purification purposes and the streptavidin had
561 no function in this work. The protein pWA comprises the C-terminal domain from the
562 WASP/Scar proteins, a ubiquitous family of proteins that initiate actin polymerization on a pre-
563 existing actin filament in the presence of the Arp2/3 complex and actin monomers.
564 Micropatterning of this actin nucleation-promoting factor was performed as previously
565 described^{22–24}. In short, glass coverslips were oxidized for 2 min with an oxygen plasma and
566 then passivated by incubating them with 0.1 mg/mL poly(L-lysine)-graft-poly(ethylene glycol)
567 (PLL-g-PEG ; Jenkem Technology) in 10 mM 4-(2-hydroxyethyl)-1-piperazineethanesulfonic
568 acid (HEPES) at pH 7.4 for 1 hour. The passivated surfaces were exposed to deep ultraviolet
569 light (wavelength: 180 nm; UVO Cleaner Unit 342; Jelight Company Inc.) for 5 min through a
570 transparent micropattern printed on a chromium synthetic quartz photomask (Toppan
571 Photomasks). The coverslips were then incubated with 1 μ M His-pWA-Streptavidin in a buffer
572 containing 50 mM KCl, 1 mM MgCl₂, 1 mM ethylene glycol-bis(β -aminoethyl ether)-
573 N,N,N',N'-tetraacetic acid) (EGTA), and 10 mM imidazole-HCl at a pH of 7.8 for 10 min. In
574 our experiments, the pattern was typically composed of 9- μ m diameter disks.

575 **Actin polymerization in the presence of myosin motors.** Actin polymerization from surface
576 micro-patterns of the nucleation-promoting factor His-pWA-Streptavidin was induced in a
577 solution containing 2 μ M globular actin (Tebu-Bio), 8 μ M profilin (produced as described in
578 ⁵⁰), 80 nM Arp2/3 complex (Tebu-Bio), and myosin molecular motors. We used one of 2 types
579 of myosin molecules. First, double-headed heavy meromyosin II—here simply called myosin
580 II, purified from rabbit pectoral muscle according to a published protocol⁵¹, was provided by
581 the group of Matthias Rief (Technische Universität München, Munich, Germany) and used at
582 a typical concentration of 500 nM (range: 250 nM-1500 nM). Second, recombinant double-
583 headed myosin Va missing the C-terminal globular tail and fused to the green-fluorescent
584 protein (GFP)—here called myosin V—was produced as described⁵² and used at a
585 concentration of 50 nM. The buffer of the acto-myosin polymerization solution was composed
586 of 10 mM imidazole-HCl (pH 7.8), 50 mM KCl, 1 mM MgCl₂, 4.2 mM disodium adenosine
587 triphosphate (ATP), 56 mM dithiothreitol (DTT), 0.1 mg/mL glucose, 42 nM catalase, 0.6 mM
588 glucose oxidase, and 0.3% (w/v) methylcellulose. Using an Ubbelohde viscometer (type Ib; SI
589 Analytics), we measured a viscosity of 15 mPa·s for this solution at 27°C. In order to visualize

590 actin filaments, 10% of the monomers were labeled with a fluorophore (Alexa568; Life
591 Technologies). A thermostat-controlled chamber ensured that experiments were performed at a
592 constant temperature of 27°C.

593 **Microscopic Observations.** Our samples were observed through a $\times 60$ objective (numerical
594 aperture:1.4) of a spinning-disk confocal microscope (Eclipse 80i; Nikon). Time-lapse videos
595 were recorded with an EMCCD camera (Ultra897 iXon) at time intervals from 0.2 to 2 s. Time-
596 lapse recordings could start as early as 5 min after the injection of the polymerization mix into
597 the flow chamber and last up to 1 hour.

598 **Image analysis.** We used the ridge-detection plugin⁵³ of the image-processing software
599 ImageJ (NIH) to automatically track the center line of actin-filament bundles. The bundles
600 appeared as bright curvilinear objects on a dark background as a result of actin fluorescent
601 labelling (Fig. 1a). Regions of interest with well-separated bundles were first selected. Only the
602 beating part of the bundle was selected. A region of interest could encompass most of the
603 bundle's length, from the border of the actin-nucleation area to the bundle's tip (Supplementary
604 Video 1; yellow box in Extended Data Fig. 1d), or be positioned some distance away from the
605 nucleation area (as in Supplementary Videos 3 and 8; yellow bow in Extended Data Fig 1f). If
606 necessary, a rotation was applied on the selected regions to orient the base of the target bundle
607 vertically. Neighboring bundles were deleted from the grayscale images to ensure that the
608 tracking procedure did not yield parasite sets of coordinates. The output of the ridge-detection
609 plugin was a stack of images, each showing the bundle's center line as a black line on a white
610 background at a given time point. In each image, we then extracted and ordered the coordinates
611 (X, Y) of the detected line. These coordinates were each smoothed using a moving average with
612 a span of 5 points, before computing the arc length s along the bundle's centerline. After a
613 linear interpolation of the relations $(X(s), Y(s))$ with an arc-length increment of $0.01\mu\text{m}$,
614 corresponding to about $1/25^{\text{th}}$ of the pixel size, we parametrized the shape of the center line
615 by computing, at each point of the line, the tangent angle $\psi(t, s)$ relative to the vertical axis (Y-
616 axis). At each time t , the relation $\psi(s)$ was then smoothed using a gaussian filter with a standard
617 deviation of 100 points, corresponding to a distance of $1\mu\text{m}$ or about $1/20^{\text{th}}$ of the wavelength
618 of the bending waves, before computing the local curvature $\psi'(t, s) = d\psi/ds$. The base of the
619 bundle was located at $s = 0$ and its tip at $s = L$, where the bundle's length $L(t)$ increased slowly
620 over time as a result of actin polymerization. The amplitude of tangent-angle oscillations
621 (Fig. 1d) was defined as $\psi_0(s) = \sqrt{2\langle(\psi(t, s) - \langle\psi(t, s)\rangle)^2\rangle}$, where $\langle\cdot\rangle$ denote a time average
622 over the duration of the recording. Their period T and phase $\phi(s)$ was obtained from the

623 frequency $1/T$ and phase at the peak of the Fourier transform $\phi(\omega, s) = \int \psi(t, s) e^{-i\omega t} dt$. We
624 then calculated the local wavelength $\lambda(s) = -2\pi/\phi'$ and velocity $v = \lambda/T$ of the actin-
625 bending waves. Myosin-density profiles $\rho(t, s)$ were obtained by computing, as a function of
626 time, the intensity of the myosin-fluorescent signal along the actin bundle's center line. The
627 speed of myosin-density wave was obtained by tracking the arc length of the myosin-density
628 peak along the bundle as a function of time, as shown in Fig. 4e (black line). Data analysis was
629 performed using custom software written in Matlab (the Mathworks).

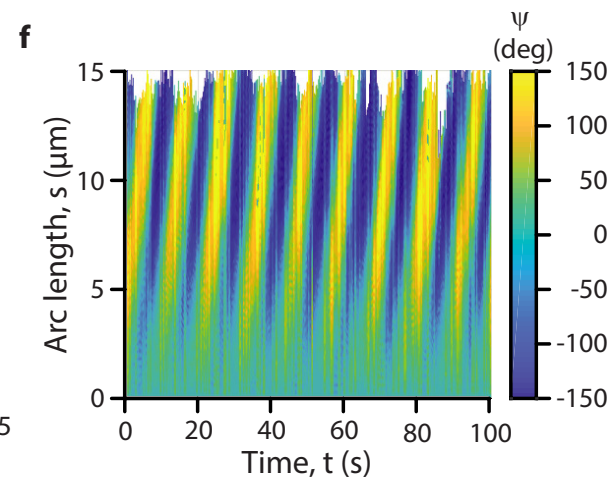
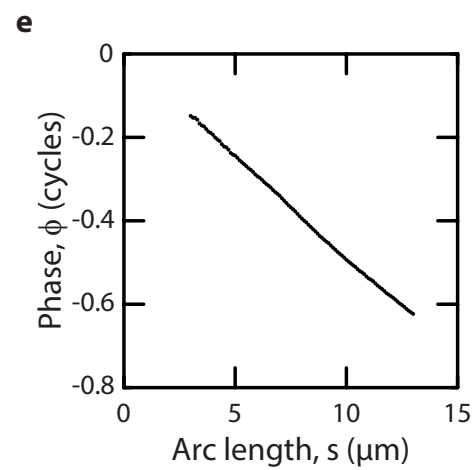
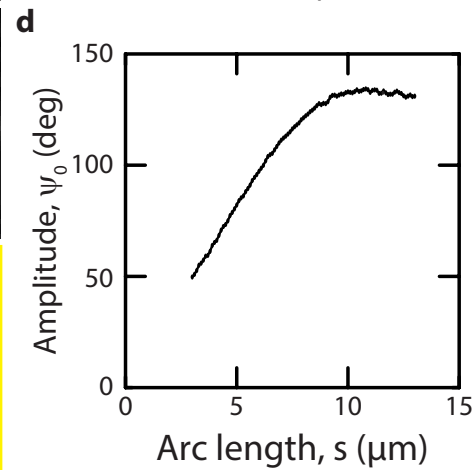
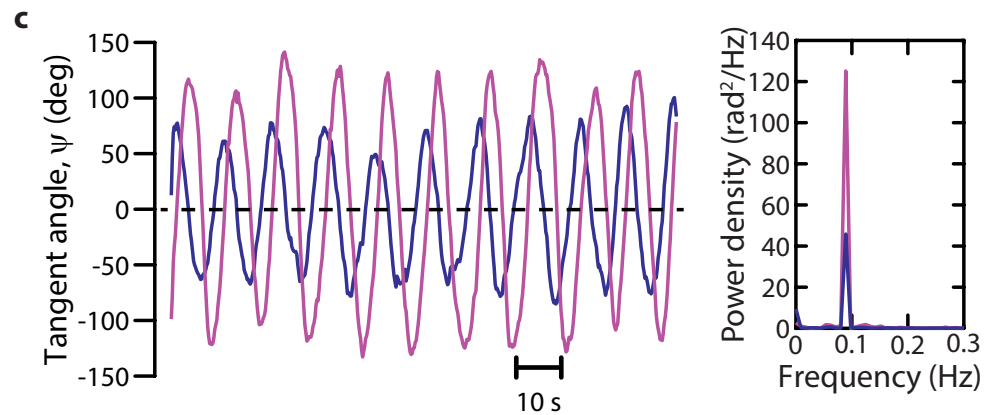
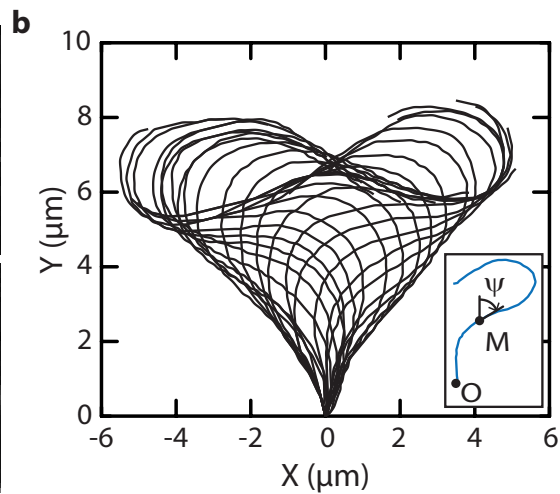
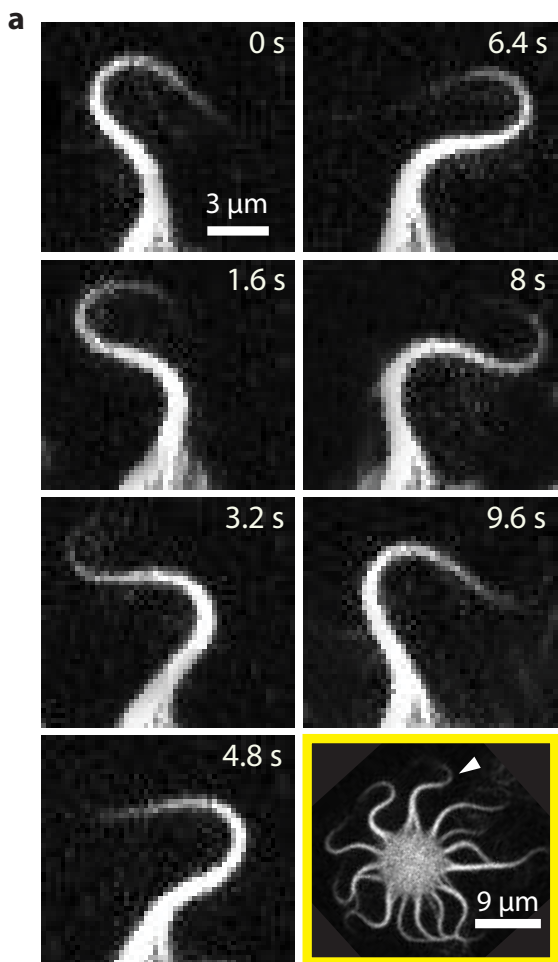
630 **Statistical testing.** Unless otherwise indicated, all the results are quoted as mean \pm standard
631 deviation over an ensemble of n actin-filament bundles. Statistical significance of the difference
632 between the means over two data ensembles, in practice data obtained with beating bundles
633 driven with myosin II and myosin V, was assessed using a two-tailed Student's t-test with
634 Welch correction. Correlations were assessed by computing a Pearson's correlation coefficient
635 and its p-value.

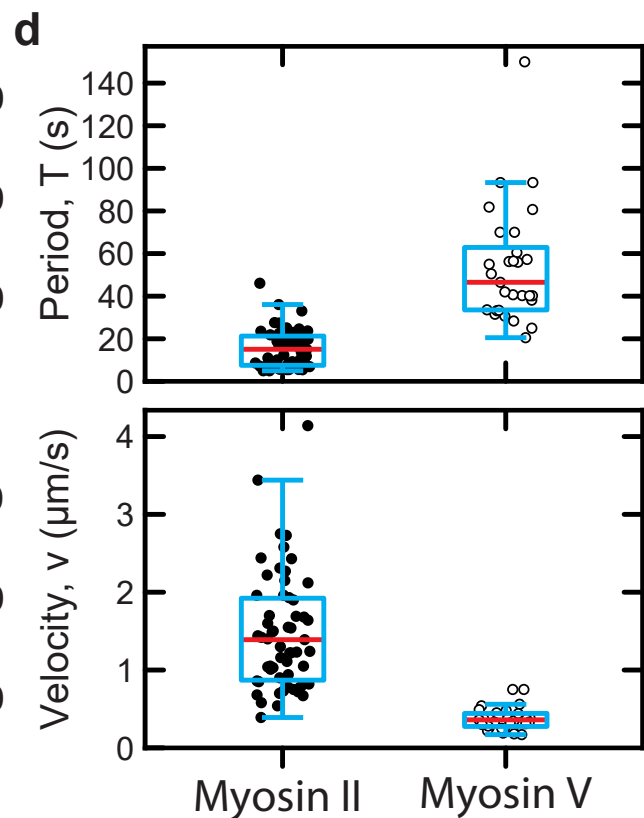
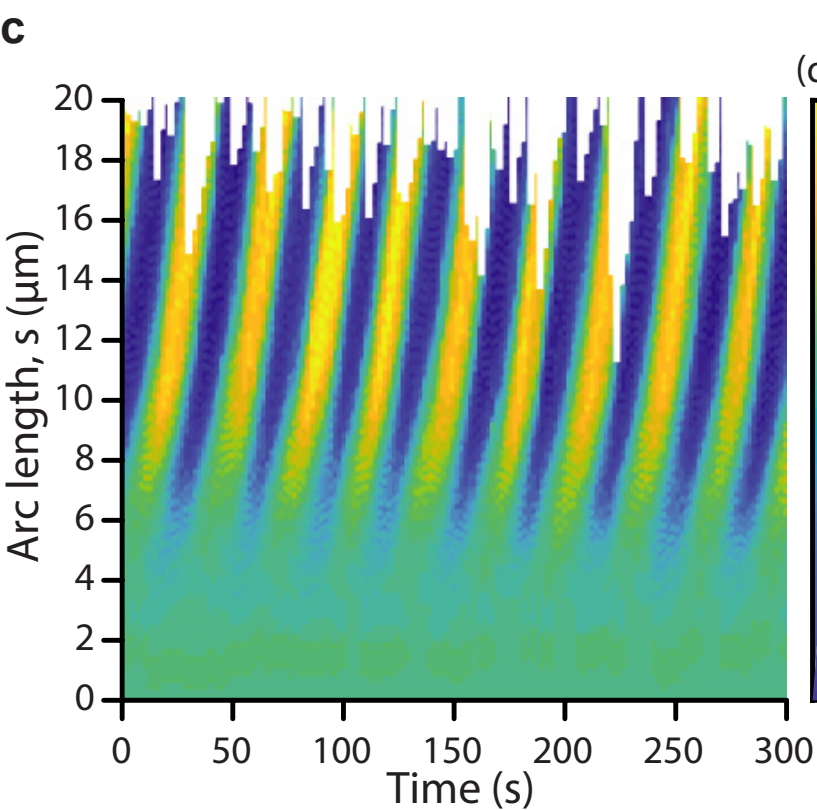
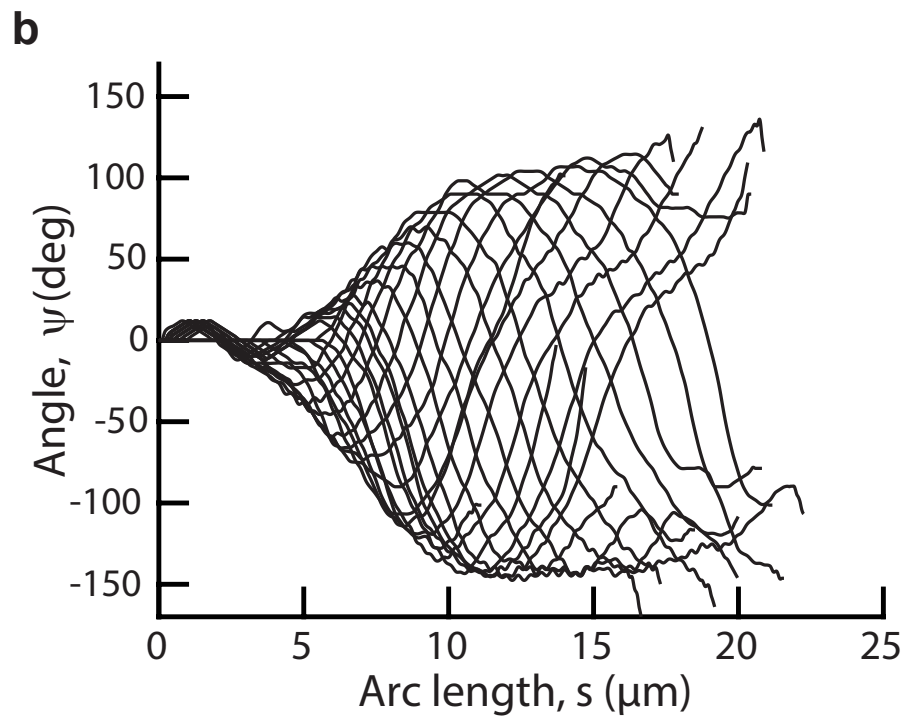
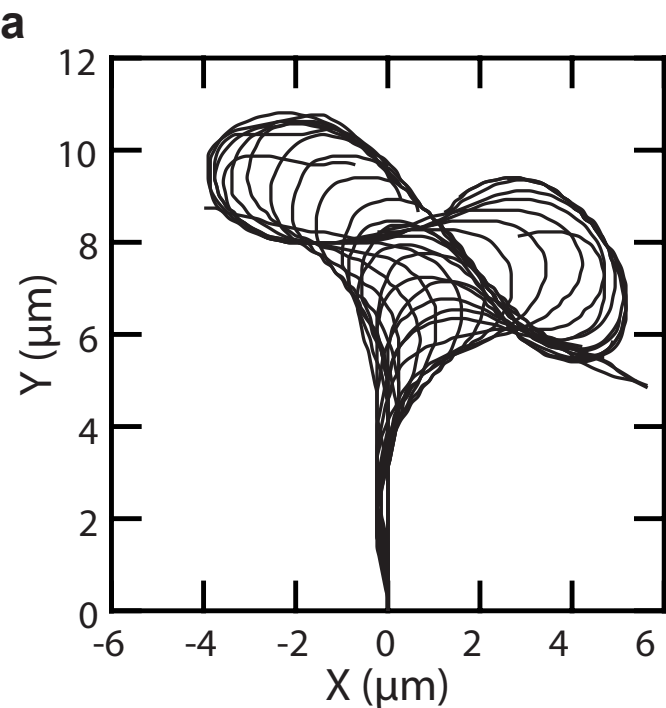
636 **Data availability statement**

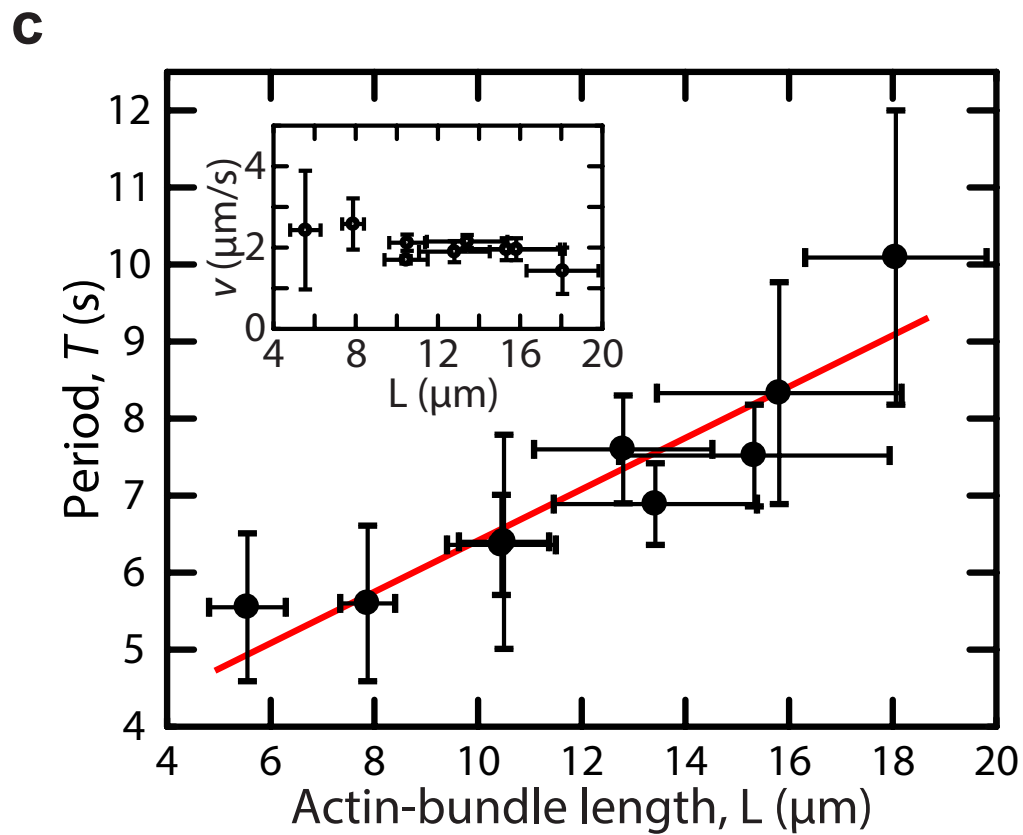
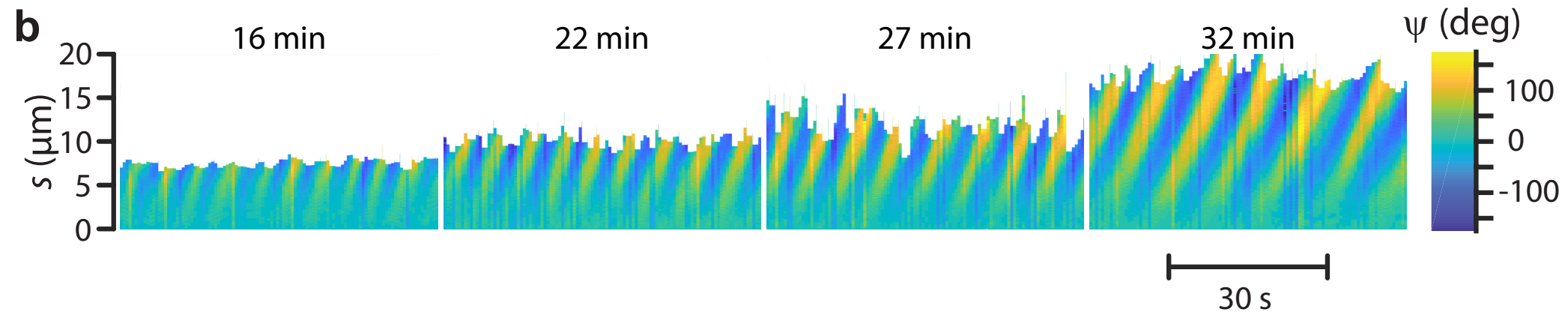
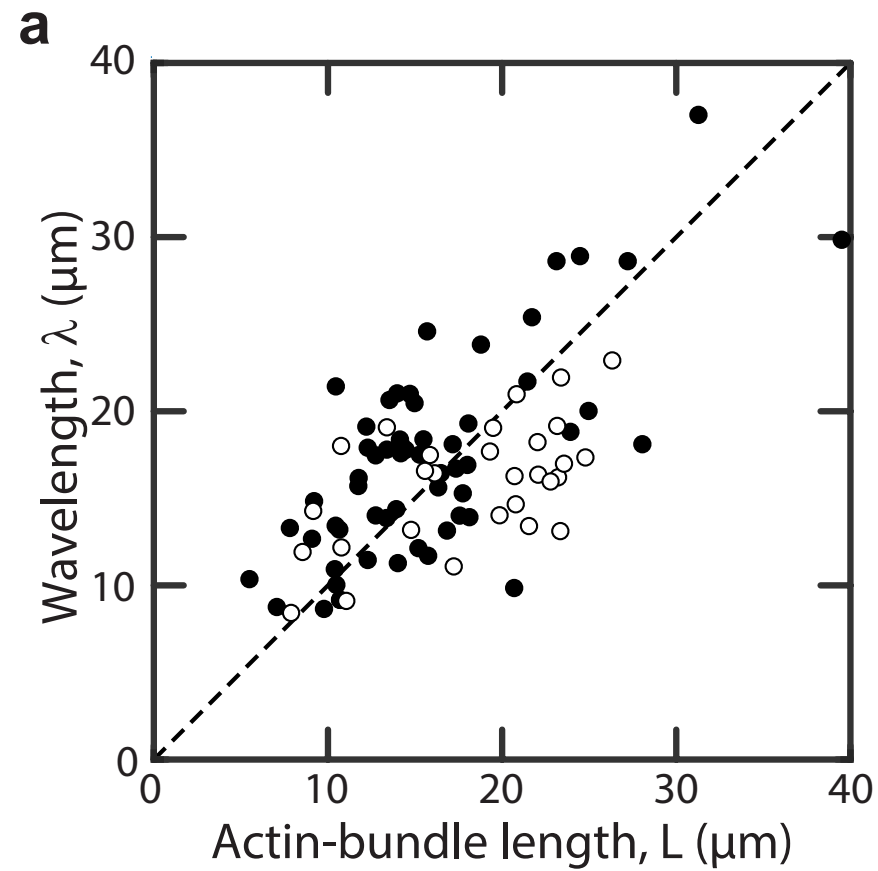
637 Source data are available for this paper. All other data that support the plots within this paper
638 and other findings of this study are available from the corresponding author upon reasonable
639 request.

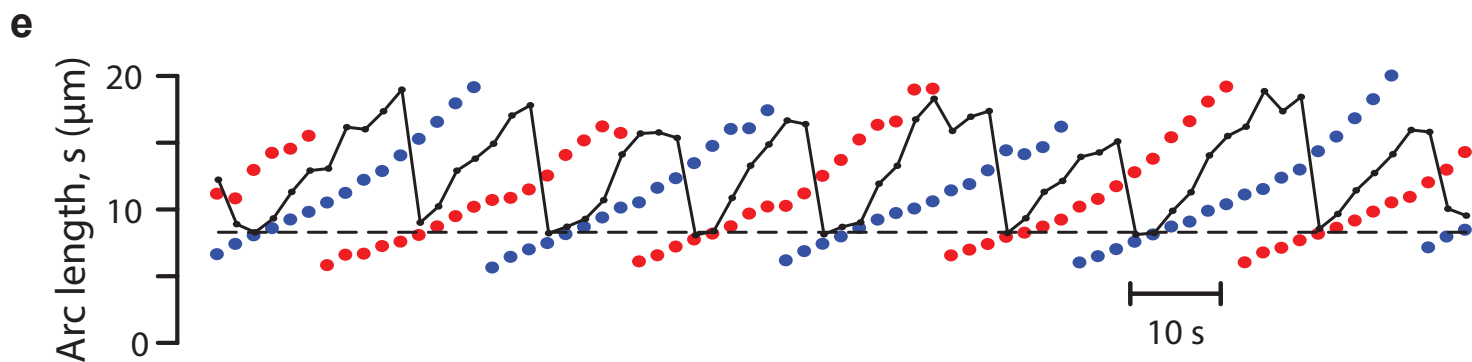
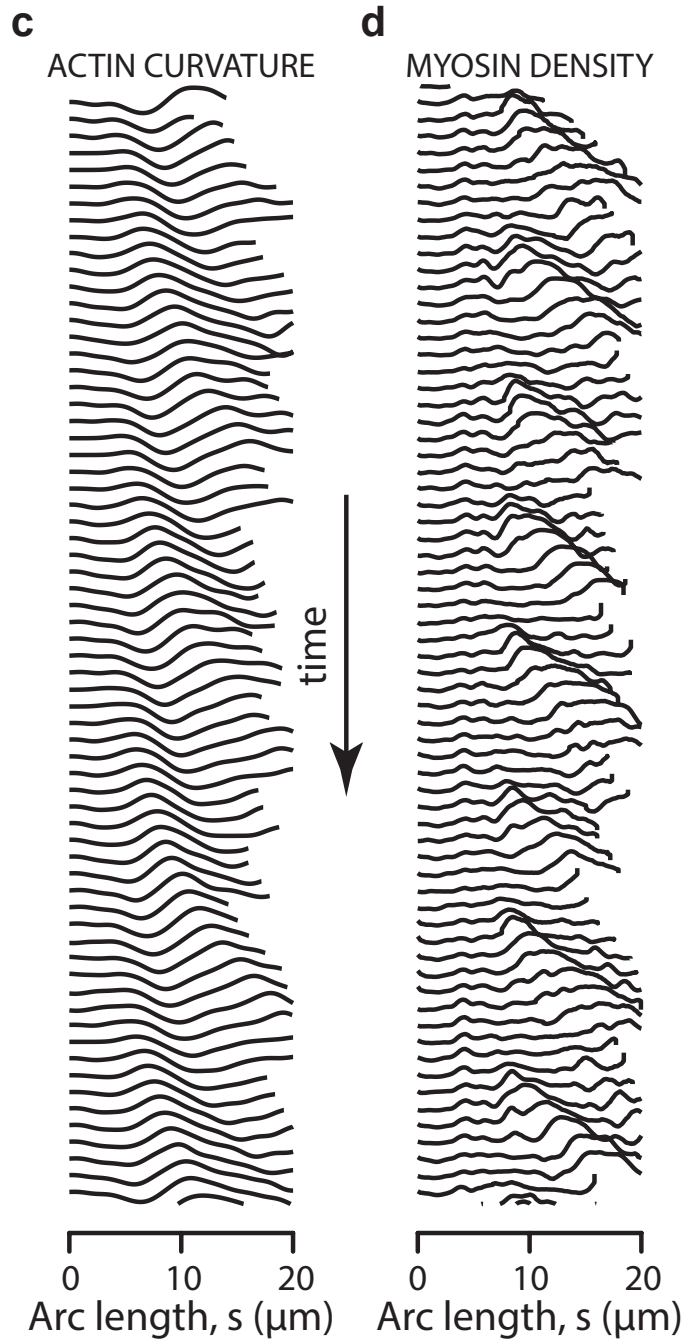
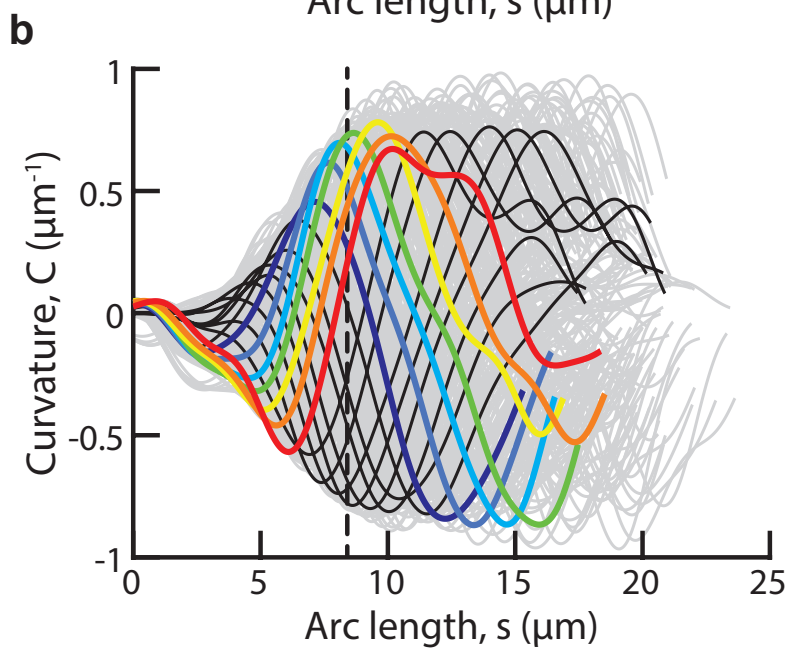
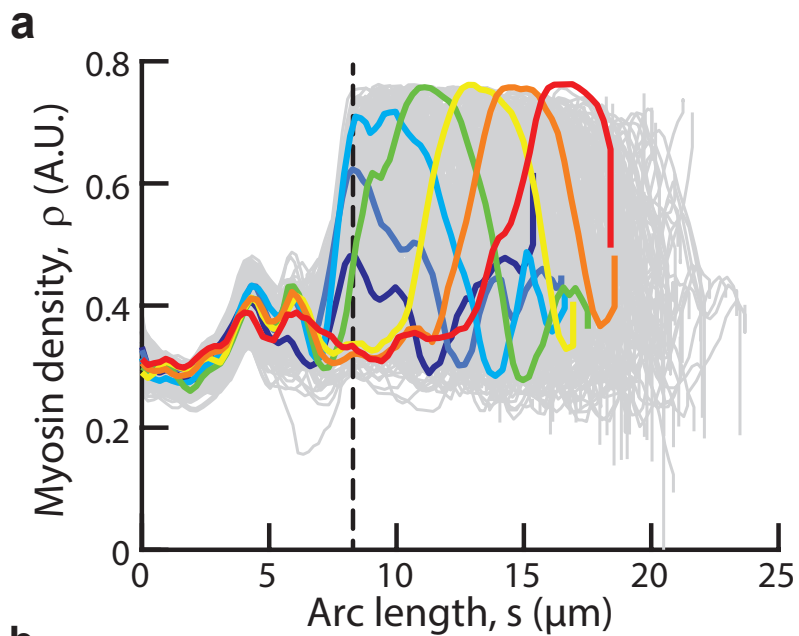
640 **References**

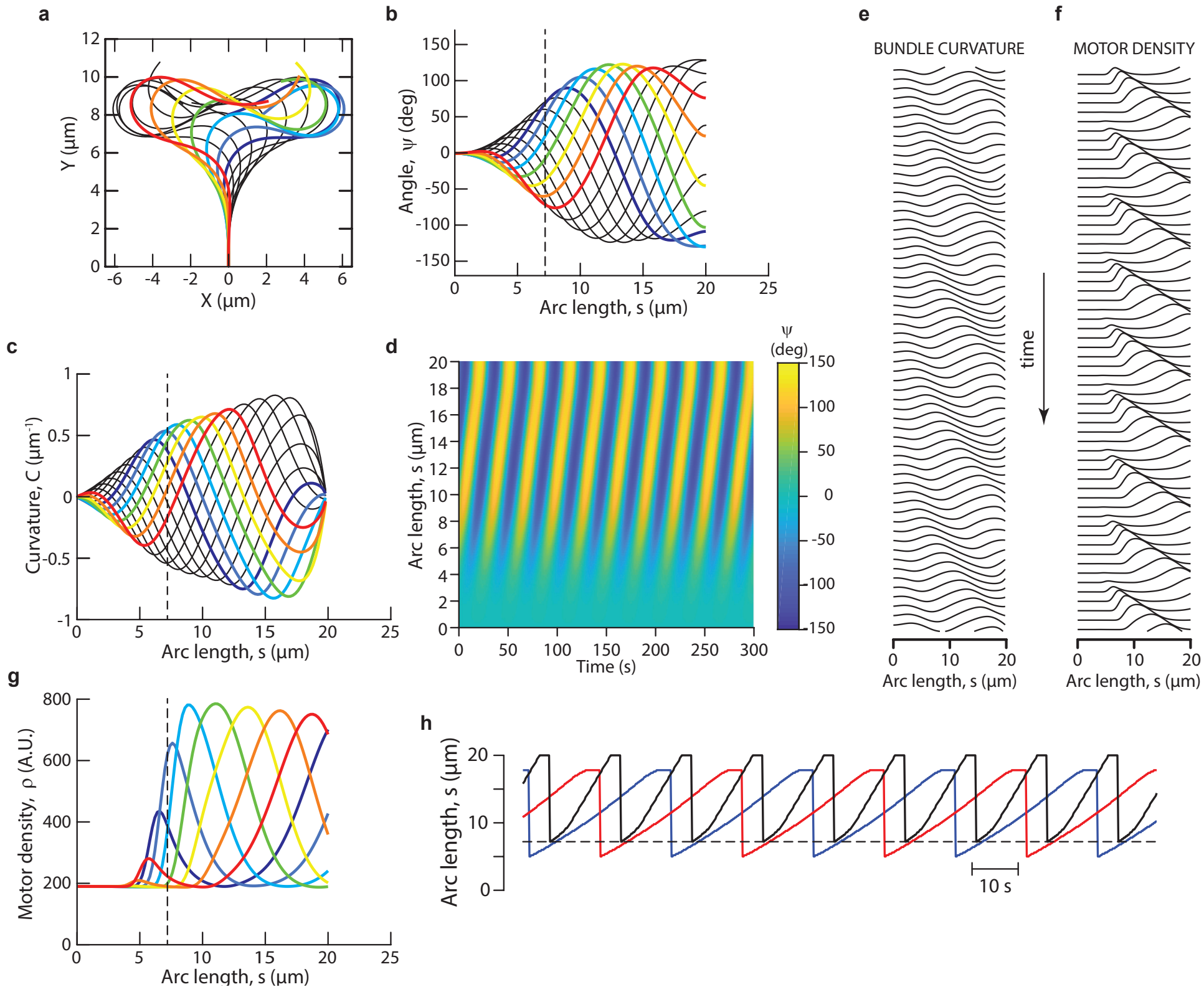
- 641 50. Carvalho, K. *et al.* Actin polymerization or myosin contraction: two ways to build up
642 cortical tension for symmetry breaking. *Philos. Trans. R. Soc. Lond. B Biol. Sci.* **368**,
643 20130005 (2013).
- 644 51. Margossian, S. S. & Lowey, S. Preparation of myosin and its subfragments from rabbit
645 skeletal muscle. *Methods Enzym.* **85 Pt B**, 55–71 (1982).
- 646 52. Snyder, G. E., Sakamoto, T., Hammer, J. A., Sellers, J. R. & Selvin, P. R. Nanometer
647 Localization of single green fluorescent proteins: evidence that myosin V walks hand-over-
648 hand via telemark configuration. *Biophys. J.* **87**, 1776–1783 (2004).
- 649 53. Steger, C. An unbiased detector of curvilinear structures. *IEEE Trans. Pattern Anal. Mach.*
650 *Intell.* **20**, 113–125 (1998).

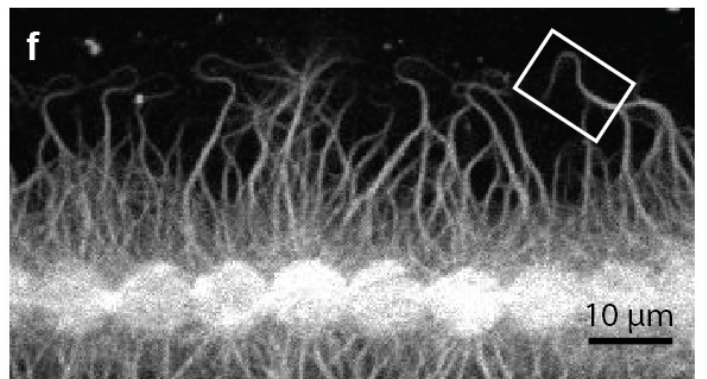
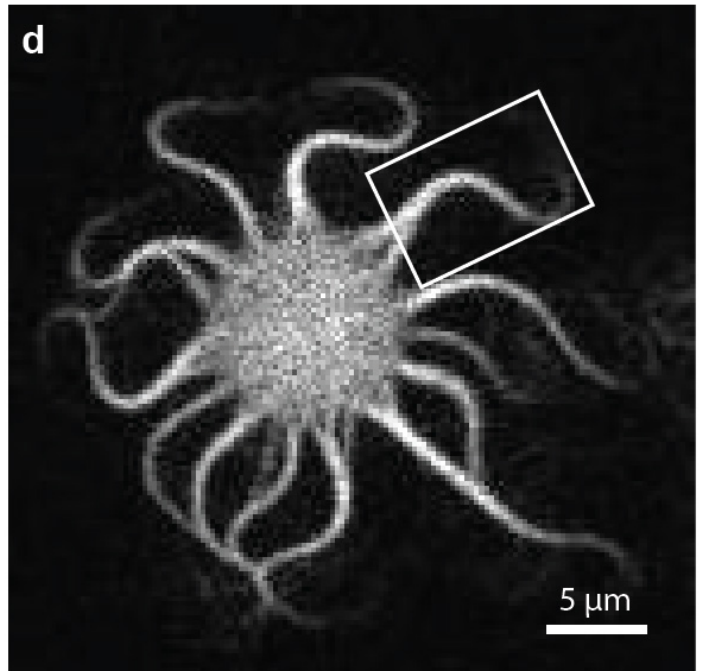
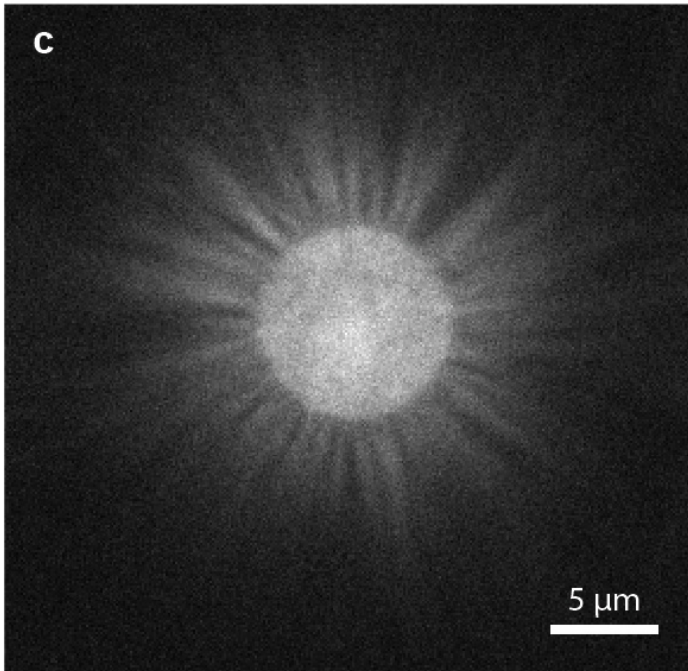
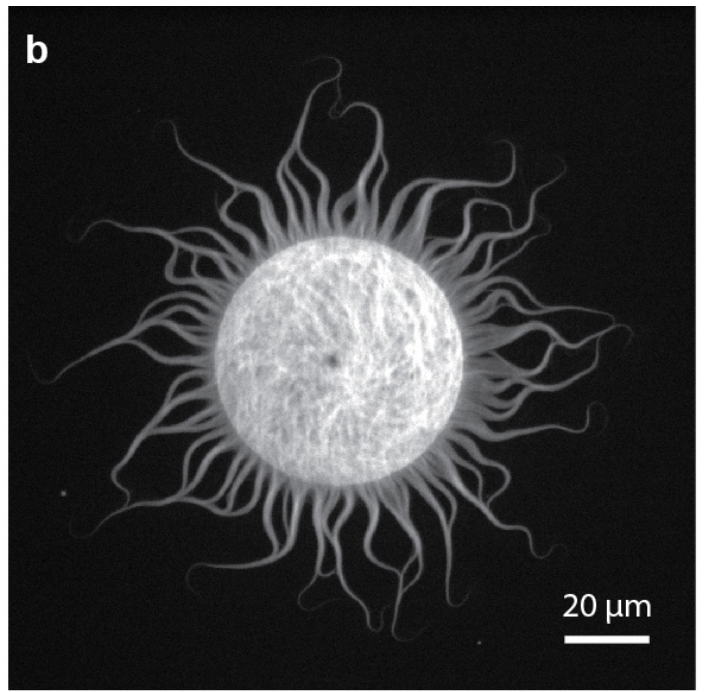
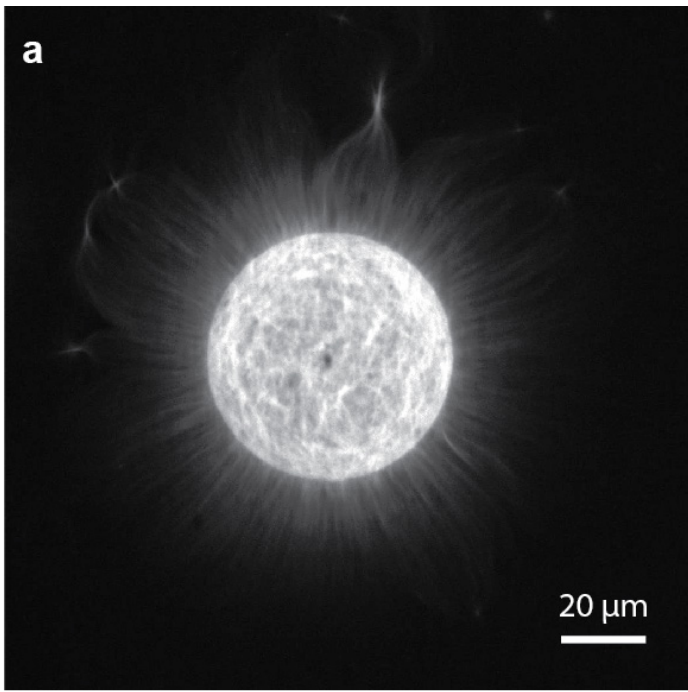


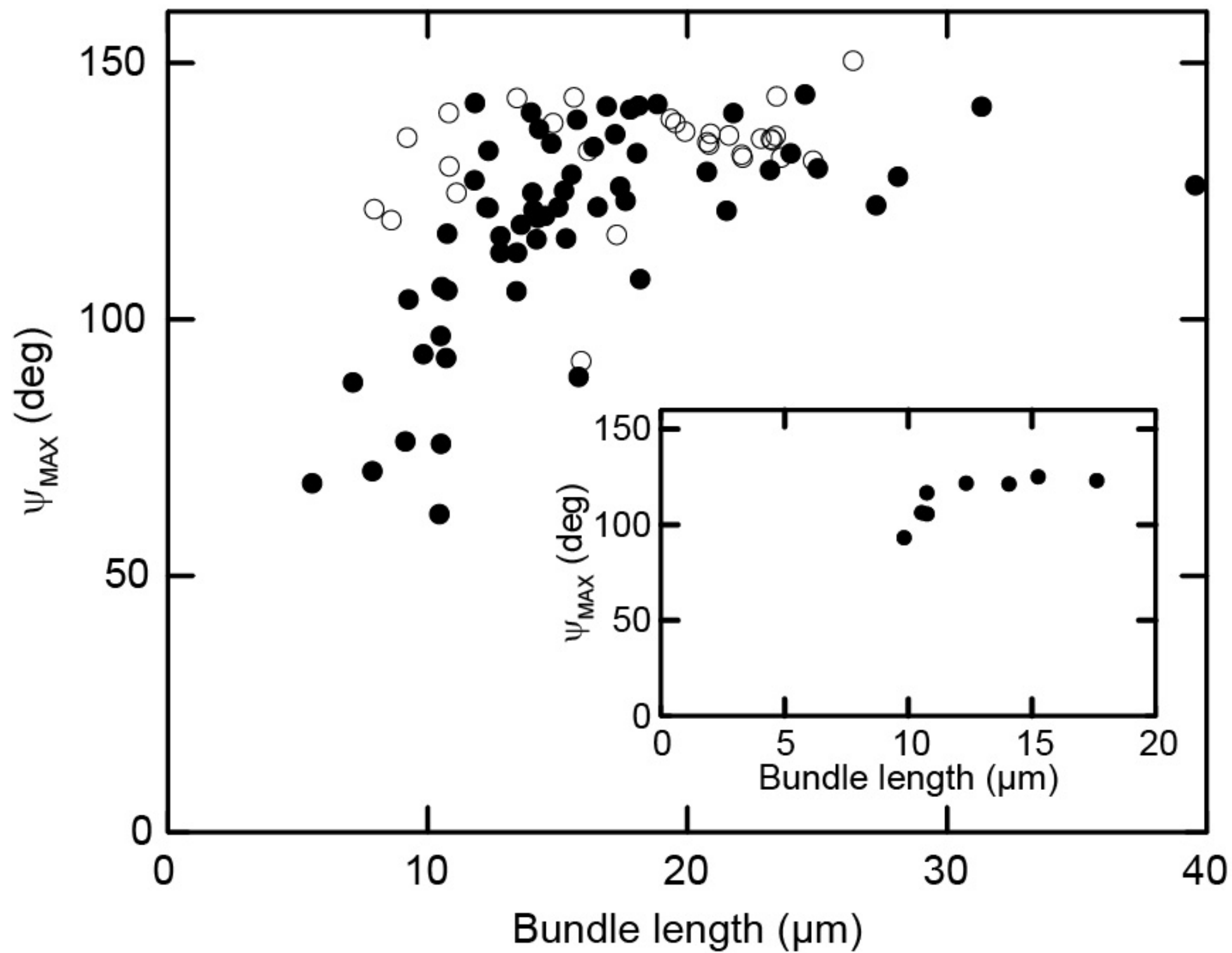


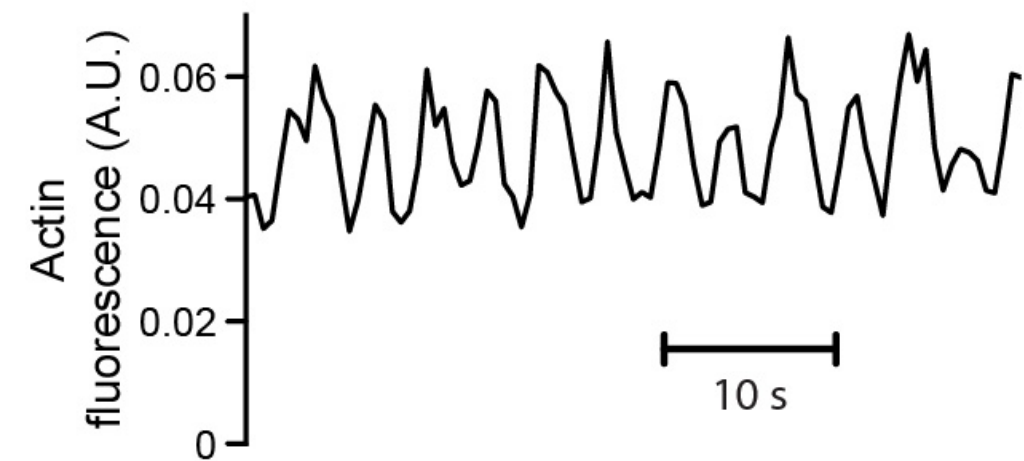
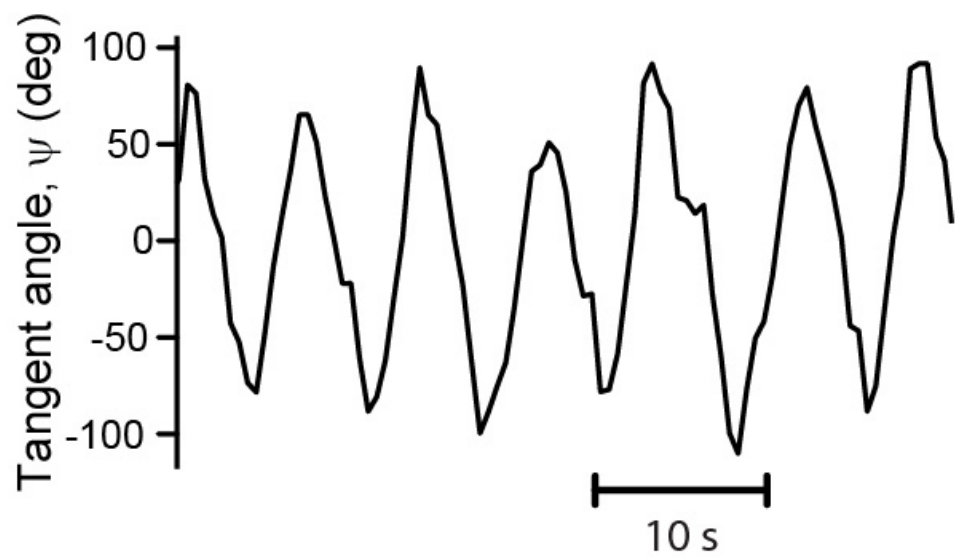
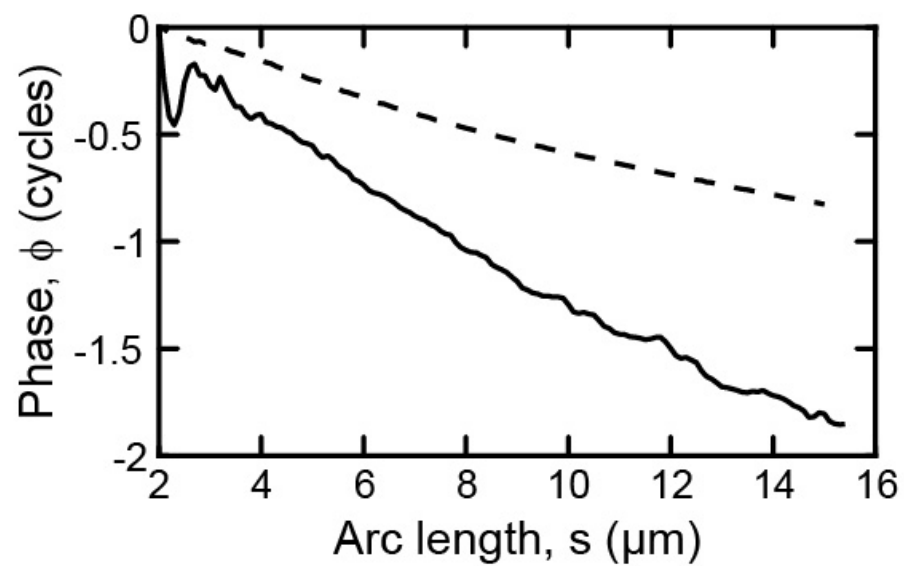
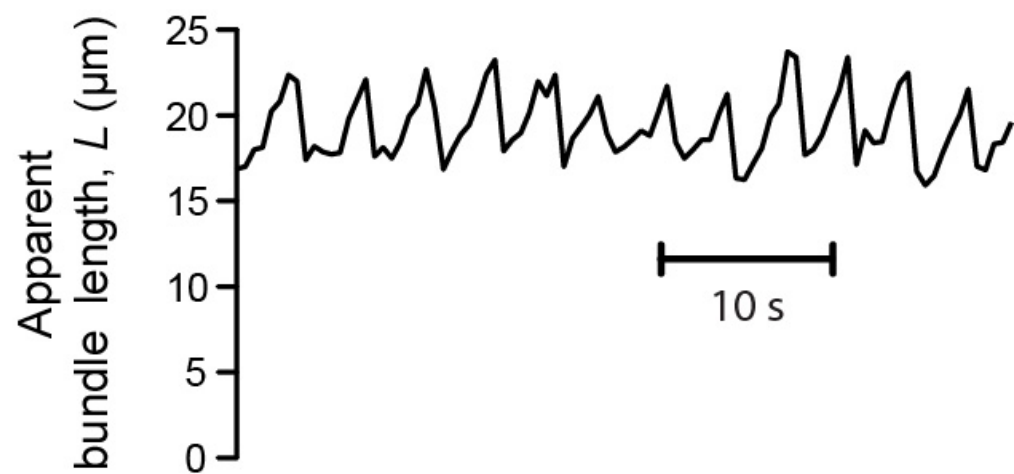


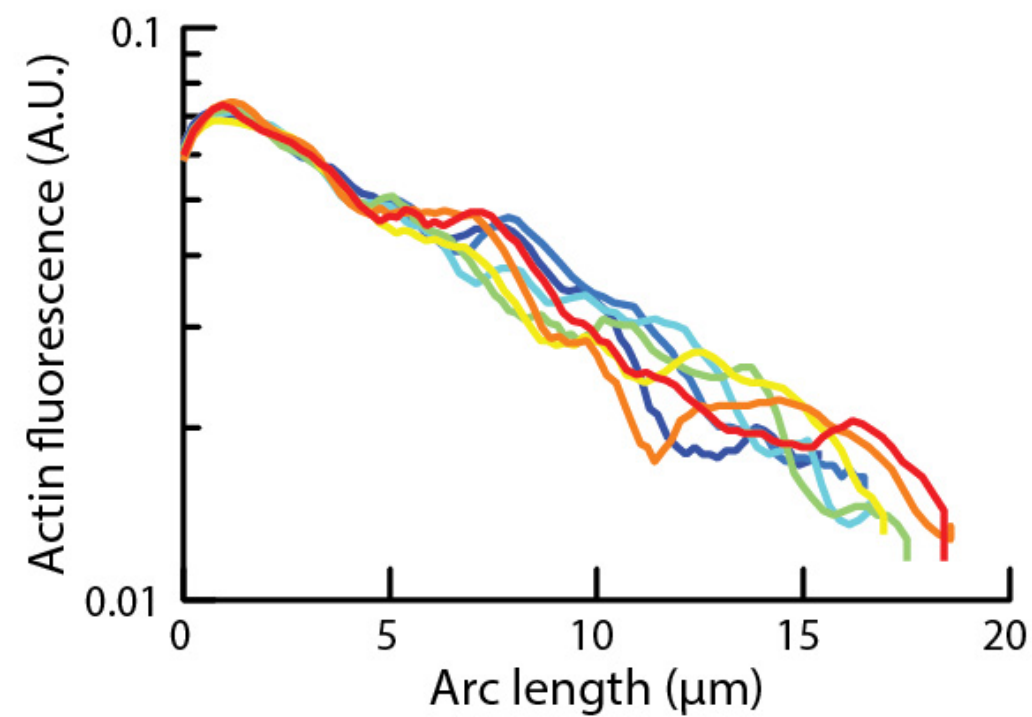
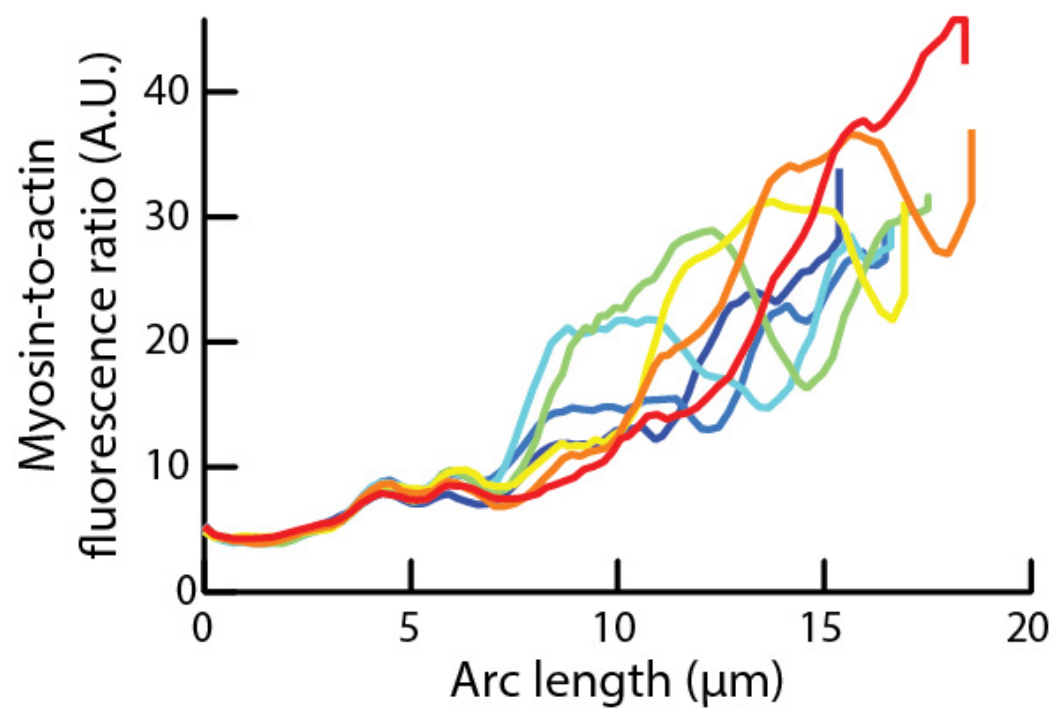


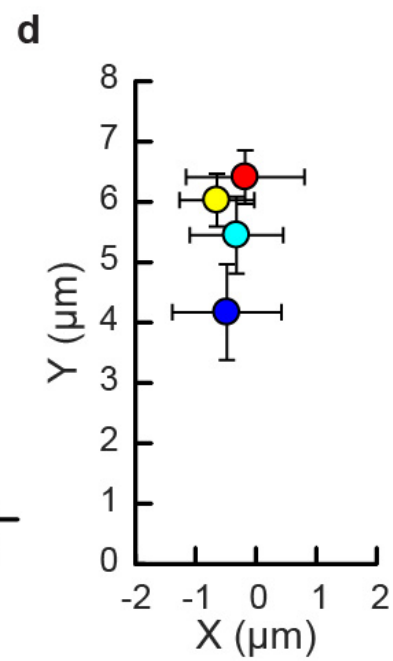
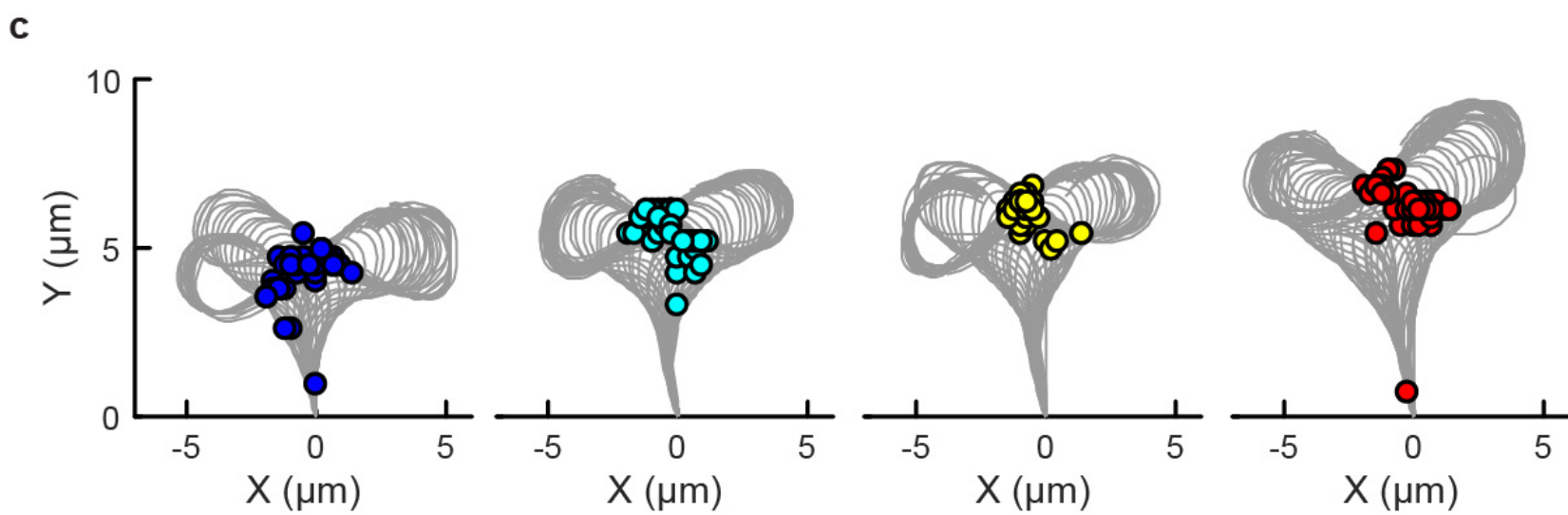
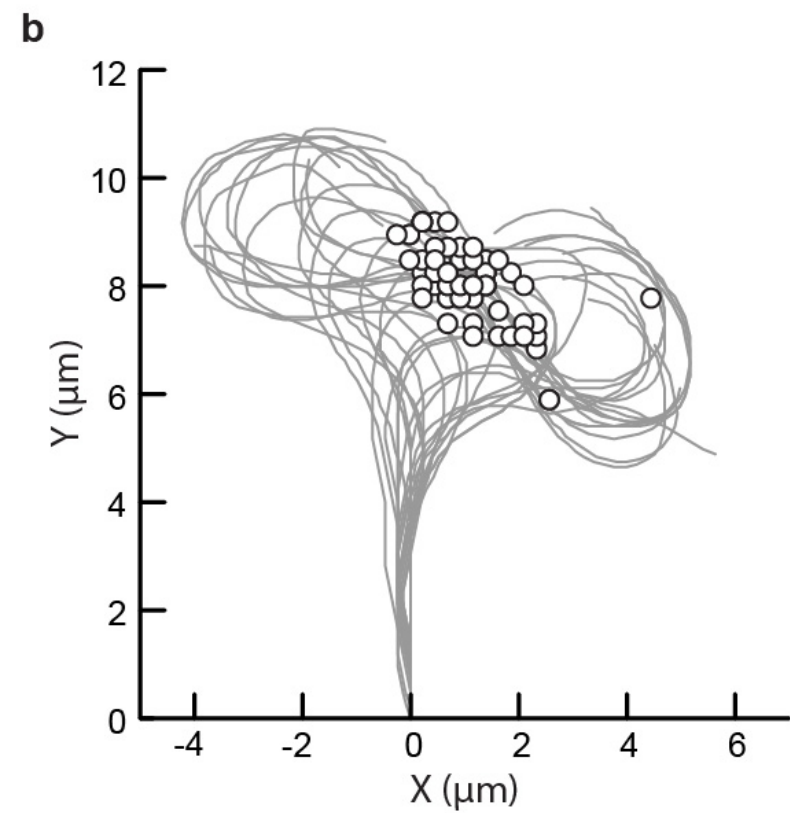
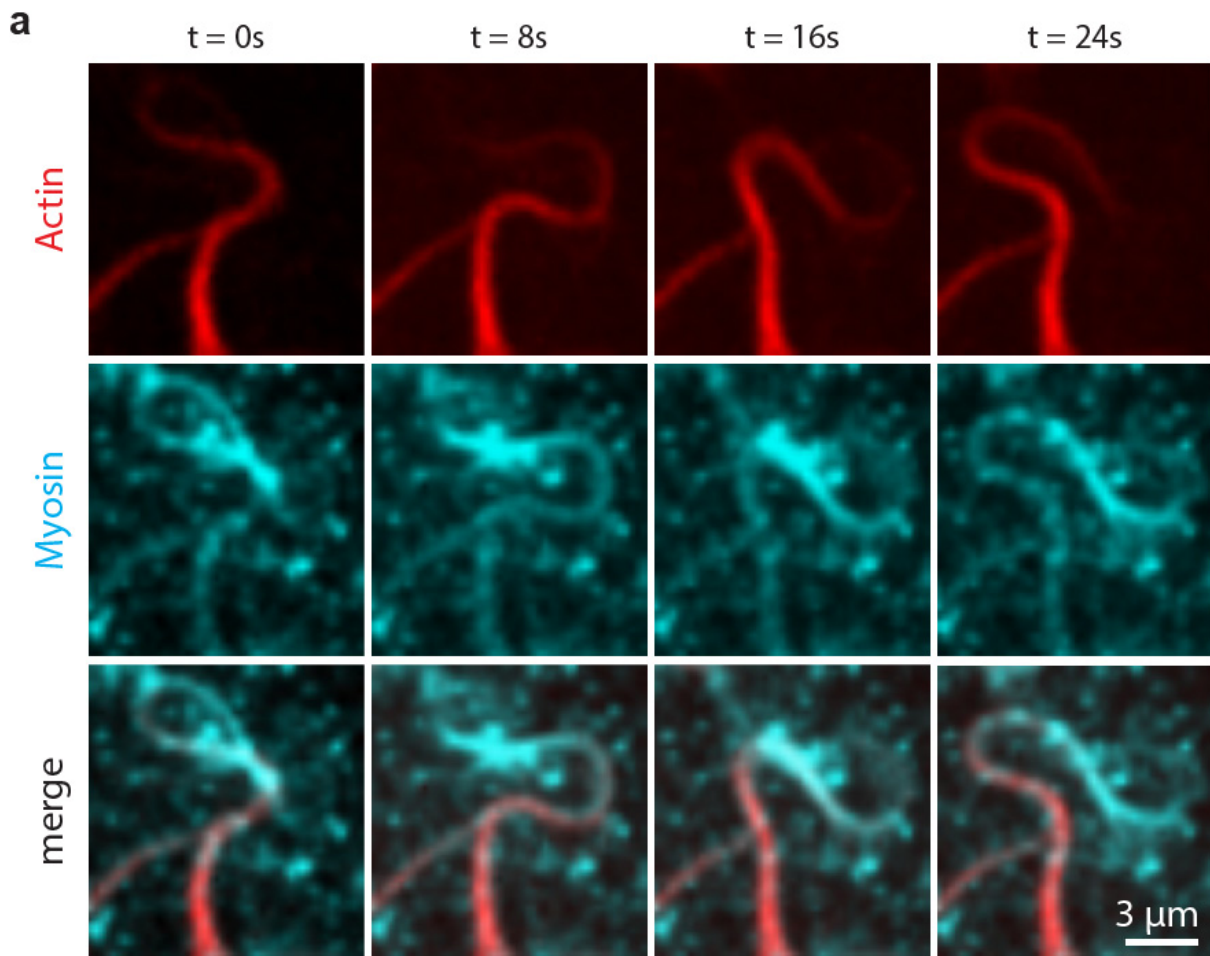


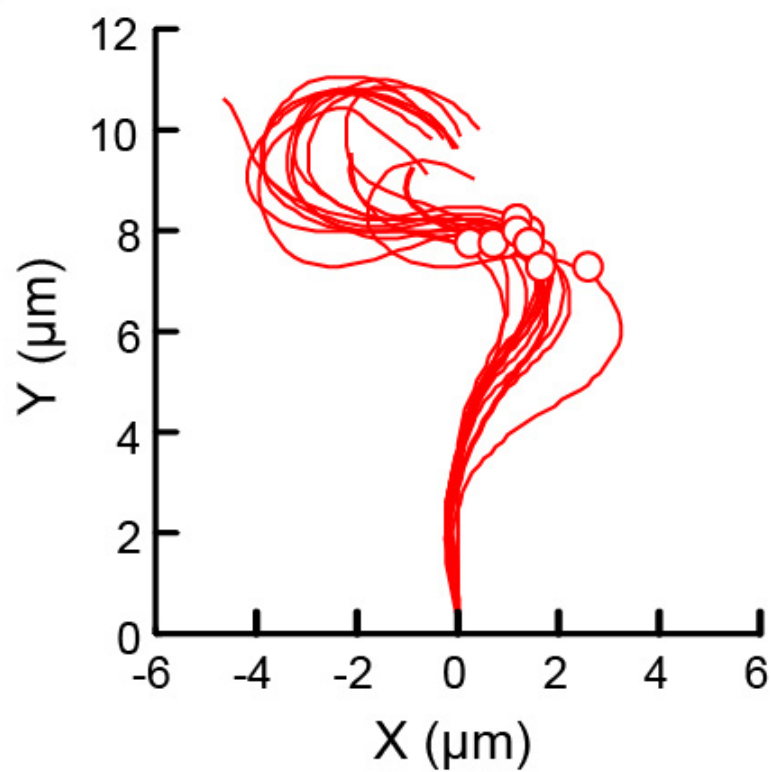
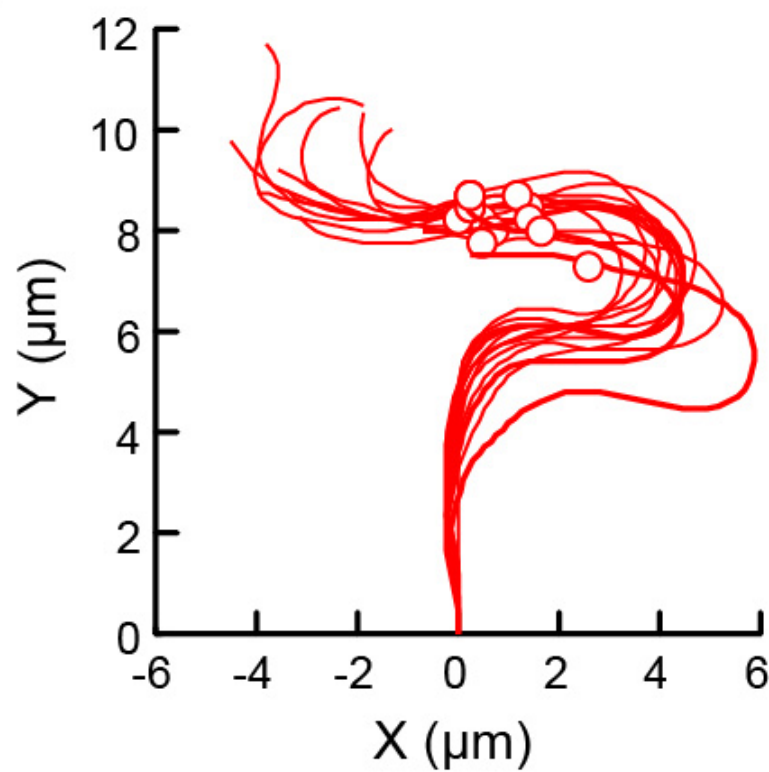
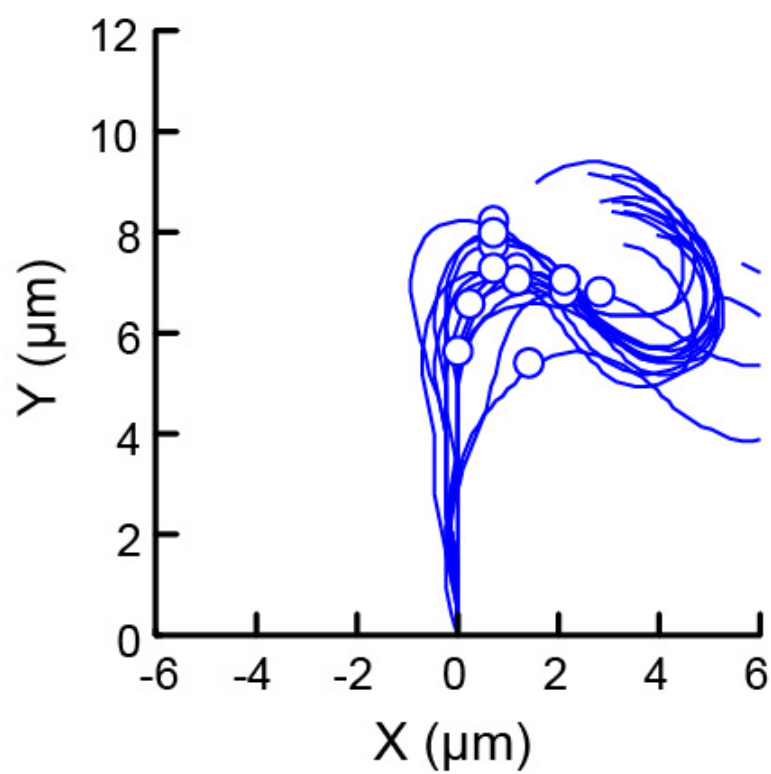




a**b****c****d**

a**b**



a**b****c****d**